JOURNAL OF COMPUTATIONAL PHYSICS **123,** 127–148 (1996)
ARTICLE NO. 0011

A Front-Tracking Method for Dendritic Solidification

DAMIR JURIC AND GRÉTAR TRYGGVASON

Department of Mechanical Engineering and Applied Mechanics, The University of Michigan, Ann Arbor, Michigan 48109

Received October 20, 1994; revised April 11, 1995

We present a front-tracking method to simulate time dependent two-dimensional dendritic solidification of pure substances. The method is based on a finite difference approximation of the heat equation and explicit tracking of the liquid–solid interface. Discontinuities in material properties between solid and liquid phases as well as topology changes and interfacial anisotropies are easily handled. The accuracy of the method is verified through comparison with exact solutions to a two-dimensional Stefan problem. Convergence under grid refinement is demonstrated for dendritic solidification problems. Experimentally observed complex dendritic structures such as liquid trapping, tip-splitting, side branching, and coarsening are reproduced. We also show that a small increase in the liquid to solid volumetric heat capacity ratio markedly increases the solid growth rate and interface instability. © 1996 Academic Press, Inc.

1. INTRODUCTION

Dendritic growth of crystals into an undercooled liquid is a very common form of solidification in castings, ingots, and welds. The microstructure produced upon solidification determines the qualities of the solidified raw material and often the finished product. This problem has attracted much interest for several years and has been motivated by the desire to predict crystalline microstructure in designing solidification methodologies for advanced materials in the aerospace and semiconductor industries, for example. Protein crystallization and igneous rock formation are just two examples of problems where researchers in fields as diverse as medicine and geology also stand to benefit from a better understanding and control of crystal growth. Despite the large volume of literature dealing with dendritic growth, the problem is still not well understood, even for the simplest case of solidification of a pure substance. Mathematical theories and numerical investigations have had only limited success in comparison with experiments. Here, we present a numerical method for solidification problems based on a simple finite difference approximation of the heat equation and explicit tracking of the liquid–solid interface. The method is general in the sense that it can handle discontinuities in material properties between liquid and solid phases, interfacial anisotropy, and topology changes. An overview of previous research on theories and simulations of morphological instabilities and dendritic solidification is given first, in order to put our work into perspective.

The process of solidification of a pure substance can occur in either a stable or an unstable manner. Stable solidification, classically called the Stefan problem, is characterized by conduction of heat away from the solid–liquid interface through the solid. The interface generally remains smooth; any protrusions of the solid into the liquid are retarded. Stable solidification is dominated by heat diffusion while surface tension and interface kinetic effects are negligible. Analytic solutions of the Stefan problem for simple geometries are well known (see, for example, [1]). Numerical methods for the solution of more complex situations include boundary fixing techniques using the Landau transformation [2] and the popular enthalpy method [3]. In the enthalpy method the interface is not explicitly tracked but must be determined after the solution has been obtained. In this respect the method is easy to use if precise knowledge of the interface location is not critical. It has received widespread use in industrial applications, where the phase change occurs over a temperature range and the melt/solid interface can be described as a mushy zone. However, Voller *et al.* [4] demonstrate that the enthalpy method produces nonphysical features when the melting temperature is sharply defined. Voller and Cross [5] propose an extension to the conventional enthalpy method which eliminates this problem and they demonstrate its applicability to one- and two-dimensional problems. More recently, Swaminathan and Voller [6] have developed a general enthalpy method which encompasses both the source-based and the apparent heat capacity enthalpy methods. From the general method they identify an optimal enthalpy scheme for a range of two-dimensional phase change problems. Comini *et al.* [7] compare the performance of several enthalpy-based algorithms. Voller and Swaminathan [8, 9] review fixed grid techniques for phase change problems and enthalpy methods in particular. Other methods for solving stable solidification problems include inverse methods such as the isotherm migration method [10], an inverse finite element method by Alexandrou [11], and finite element methods using a deforming mesh [12].

0021-9991/96 $12.00

Unstable solidification of a pure substance takes place when the liquid is cooled below its equilibrium solidification temperature. Heat is conducted away from the solid–liquid interface through the liquid. Any local protrusion on the interface that extends into the liquid will be enhanced since the magnitude of the temperature gradient at the protrusion is greater than that at adjacent portions of the interface. The process is inherently unstable and the protrusion will grow until constrained by surface tension and interface kinetic effects. Morphologically complex dendritic structures result from this competition between surface tension and undercooling. Understanding and modeling the mechanisms which produce these structures has been the focus of much research.

The primary instability mechanisms of a steadily advancing planar interface were analyzed by Mullins and Sekerka [13] and Voronkov [14]. A similar linear stability analysis was performed for growing spheres by Mullins and Sekerka [15] using a quasi-stationary assumption that has been extended to include interface kinetics [16, 17]. Steady state models of dendrite growth are based on Ivantsov's solution [18] of the heat transport equation for a paraboloidal, isothermal interface growing at constant velocity into a uniformly undercooled liquid. For a given undercooling, an infinite number of solutions are given by combinations of the growth speed, V, and the tip radius, R, according to the relationship $VR = \text{const}$. However, this set of solutions is clearly inconsistent with the thermodynamic constraint of a minimum radius below which no growth can occur. The Ivantsov model also does not take into account effects due to surface tension and interface kinetics. Temkin [19], Bolling and Tiller [20], Trivedi [21], and Glicksman and Schaefer [22, 23] addressed these problems by including surface tension effects. Similar to Ivantsov's result, an infinite number of solutions are given in terms of $V - R$ combinations. However, for a given undercooling the curves exhibit a maximum velocity which was thought to be the unique operating state of the dendrite. Unfortunately, the tip radii predicted by the maximum velocity hypothesis do not agree well with experimental observations [24]. Nash and Glicksman [25] formulated a self-consistent free boundary problem in the form of a nonlinear integrodifferential equation. Solution of this equation [26] yielded only a slight modification to Ivantsov's paraboloid shape and results similar to the maximum velocity hypothesis.

Time dependent theories for morphological instability were developed in response to the shortcomings of the steady state models. The concept of marginal stability was established by Langer and Müller-Krumbhaar [27–30]. They assumed that the operating state of the dendrite tip lies at the margin of the linearly stable and unstable states. The analysis resulted in a second relation between V and R which, together with Ivantsov's solution, determines a unique operating state. The marginal stability theory has come under question in light of recent measurements of dendrite tip velocities in pure succinonitrile in microgravity by Glicksman *et al.* [31, 32]. In addition, Glicksman and Marsh [24] contend that the marginal stability theory cannot be considered as providing a fundamental theory of dendritic crystallization due to limitations concerning the validity of both its theoretical and mathematical foundations.

More recent theories which attempt to address the concern over marginal stability resulted in advanced analytical and numerical approaches to the solution of the Nash–Glicksman integrodifferential equation and variants of this equation. The role of anisotropy of the interfacial energy in providing a selection mechanism for the dendrite operating state was used to find solutions of the anisotropic form of the Nash–Glicksman equation. These so-called microscopic solvability theories are reviewed by Kessler *et al.* [33, 34], Langer [35, 36], Pelcé [37], Gollub [38], and Kurz and Trivedi [39]. These theories and a related method by Miyata *et al.* [40] are not supported by recent experiments on camphene, pivalic acid, and succinonitrile by Rubinstein and Glicksman [41, 42] and there is still a debate over whether anisotropy of the interfacial energy provides a fundamental physical basis for the dendrite operating state selection [24].

Numerical methods for dendritic solidification problems are not as common as those for Stefan problems, due primarily to the difficulties involved in handling the complex, unstable interface shapes. Several numerical simulations, mostly in two dimensions, have, however, been successful in obtaining qualitative agreement with observed dendritic structures. Sullivan *et al.* [43, 44] use a finite element method with a deforming mesh and a careful numerical treatment of interface curvature to perform two-dimensional simulations. They have also modified this method to include anisotropic material properties [45]. In spite of the two-dimensional limitations, they obtained good agreement with experimental observations of dendrite tip velocities as a function of tip curvature. Tacke [46] applied a finite-difference enthalpy method to the 2D dendritic solidification problem. Although his results exhibit qualitatively realistic phenomena, the fourfold symmetry of the dendritic structures in his simulations is due to a canalization effect of the grid and not to any physical anisotropy. Sethian and Strain [47] use a level set approach to determine the solid/liquid boundary and include effects of anisotropic surface tension and interface kinetics. Almgren [48] uses a variational algorithm to perform similar computations. The interface is tracked and its shape is determined by minimizing an energy functional made up of bulk and surface energy contributions. The interface temperature condition is only approximately satisfied at each time step in this method. Roosen and Taylor [49] introduce a front-

tracking scheme which avoids direct computation of interface curvature by assuming that the interface is a polygon. They admit, however, that their method contains an inherent grid-induced anisotropy which is present even at high grid resolutions. Shyy *et al.* [50] have used an interface tracking method for the solution of stable and unstable solidification problems in which they map the governing equations into curvilinear coordinates. For the unstable problem, they use scaling arguments to decompose the domain into an inner region where interface perturbations develop and an outer region where the interface is assumed to be planar. The two regions are coupled by matching of the boundary conditions. Brattkus and Meiron [51] have developed an efficient algorithm to compute one-dimensional free-boundary problems using a boundary integral formulation. Their method can handle the general problem of unequal thermal diffusivities between the liquid and solid phases. They have applied the method to study oscillatory instabilities in rapid directional solidification.

Phase-field models and their numerical implementation are currently the subject of considerable interest. Langer [52], Fix [53], Caginalp [54–56], Caginalp and Fife [57], and Collins and Levine [58] have extensively studied and adapted this method. A phase-field variable ϕ is postulated which identifies the phase of a point in the domain. If the point lies in the liquid region, $\phi = 0$; if the point lies in the solid region, $\phi = 1$. Values of ϕ between zero and one represent points that lie in the interface. An evolution equation for this scalar function, consistent with the second law of thermodynamics, is coupled to a modified heat equation. Solution of this system of equations provides values of the temperature and the phase-field variable and thus, implicitly, the interface location. The main advantage of this approach is that complex topology changes are easily handled since there is no need to explicitly track the interface or even provide interfacial boundary conditions. The disadvantage of this method is in relating the parameters in the evolution equation for ϕ to phenomenological parameters such as surface tension and interface kinetic coefficient. Caginalp [55] has shown that the classical phenomenological boundary conditions of solidification are recovered under certain limits of the phase-field equations. Caginalp and Socolovsky [59, 60] conducted spherically symmetric calculations using the phase-field model. Their work provided numerical verification of the concept of a critical radius and qualitative agreement with single needle crystals. Impressive two- and three-dimensional numerical computations by Kobyashi [61–63] reveal qualitatively correct large-scale features of dendritic structures. However, the simulation parameters had to be carefully adjusted to produce the desired structures and Wheeler [64] demonstrates that small-scale features of Kobyashi's calculations such as liquid trapping and tip splitting events are crucially dependent on the mesh used. There is still debate over the thermodynamic basis of some of the phase-field models currently in use and their relation to interfacial dynamics [65, 64]. Penrose and Fife [65] and more recently Wang *et al.* [66] have developed thermodynamically consistent phase-field models based on an entropy functional. Wheeler *et al.* [67] and Murray *et al.* [68] have used the phase-field model of Wang *et al.* to critically assess the computational viability of phase field models. For two-dimensional computations of anisotropic nickel dendrites they find that their results are in good agreement with the Ivantsov and microscopic solvability theories for a given phase-field parameter which determines the interface thickness. The results, however, are dependent on the interface thickness. They suggest that, at present, realistic phase-field computations suffer from the inability to sufficiently resolve the interface. An investigation of the interface resolution problem in phase-field models using linear stability analyses is the subject of recent work by Braun *et al.* [69].

Although significant advancements in describing and understanding the mechanisms of morphological instability have been made in the past several decades, it is clear that no single unifying theory is available which can accurately predict the microstructure of unstable solidification. Numerical schemes are mostly limited to simulations of the qualitative features of dendritic growth. The aim of the present work is to provide a new numerical tool with which to study and identify the mechanisms of dendritic growth and instability under a large range of conditions. The front-tracking method described in the next section is general in the sense that it can easily handle discontinuous material properties between the liquid and solid phases, topology changes, and anisotropy of interfacial energy and kinetics. We take a direct approach to the numerical simulation of the governing phenomenological equations and interface conditions. Solutions for the heat flow and interface motion are fully coupled at each time step. Front-tracking explicitly provides the location of the interface at all times and the Gibbs–Thomson condition on the interface temperature is also explicitly satisfied. In this way we avoid introducing nonphysical simulation parameters. Undercooling, surface tension, kinetic mobility, and the thermal conductivity and volumetric heat capacity ratios between liquid and solid directly control the solution. In Section 3, we discuss results using this method for both stable and unstable solidification problems. We first compare numerical results to an exact solution of the stable Stefan problem of solidification by a line heat sink. For unstable dendritic solidification we assess the validity of the results through grid refinement studies and comparison with theories for nucleation and limiting solid fraction. We also identify the effect of discontinuous material properties on the interface growth rate and stability.

2. FORMULATION AND NUMERICAL METHOD

We consider a square, wall bounded two-dimensional domain in which we are interested in describing the solidification of a pure substance and the evolution of the liquid–solid interface. In the dendritic solidification problem, a small seed of solid is introduced into an undercooled liquid. Initially, the temperature everywhere in the solid is assumed to be equal to the equilibrium fusion temperature T_m and the temperature in the surrounding liquid is assumed to be T_∞. Thus the liquid is undercooled by an amount $T_\infty - T_m$. The densities of the liquid and solid phases are assumed to be equal and constant. Volume contraction and expansion, as well as fluid convection effects, are thereby neglected. The thermal conductivity and volumetric heat capacity of each phase are constant but not necessarily equal. A formulation employing a single heat equation can be written for both phases as long as the jumps in material properties and the liberation/absorption of latent heat at the interface is correctly accounted for. In conservative form the heat equation is

$$\frac{\partial(cT^*)}{\partial t} = \nabla \cdot k\nabla T^* + Q, \tag{1}$$

where T^* is the temperature field and c and k are the volumetric heat capacity and thermal conductivity, respectively. Q is an energy source term which accounts for the liberation or absorption of latent heat at the liquid–solid interface:

$$Q = \int_f q\delta(\mathbf{x} - \mathbf{x}_f)\, da; \tag{2}$$

q is the heat source at the interface and $\delta(\mathbf{x} - \mathbf{x}_f)$ is a three-dimensional delta function that is nonzero only at the interface where $\mathbf{x} = \mathbf{x}_f$. Since the above integral is over a surface, the source term, Q, is still a delta function. The above formulation is not new and has been used, for example, by Lightfoot [70] in analytic solutions to phase change problems and more recently in source-based enthalpy methods [6]. The treatment of the interface source term, Q, is of crucial importance to numerical solutions which use the phase change formulation in Eq. (1). As we describe below, the front-tracking method presented here allows a detailed description of the interface microstructure which is of primary interest in dendritic solidification problems.

The expression for the interface heat source, q, is a variation of the classic Stefan condition which accounts for the discontinuous heat capacity across the phases and is derived in [71]:

$$q = [L + (c_l - c_s)(T_f^* - T_m)]V. \tag{3}$$

L is the volumetric latent heat of fusion, c_l and c_s are, respectively, the liquid and solid volumetric heat capacities and T_f^* is the interface temperature, $T^*(\mathbf{x}_f(t))$. $V = (d\mathbf{x}_f/dt) \cdot \mathbf{n}$ is the normal velocity of the interface, where $\mathbf{n}$ is the normal to the interface. The term in the brackets in Eq. (3) can be thought of as a temperature dependent latent heat due to the effects of discontinuous heat capacity and the fact that the phase change generally occurs at a temperature, T_f^*, different than the equilibrium melting temperature, T_m.

In addition, the Gibbs–Thomson temperature condition must be satisfied at the interface. A thermodynamic analysis of phase coexistence at a curved interface reveals terms in the Gibbs–Thomson condition which account for the effect of discontinuous heat capacity. This expression, derived in [71, 72], is

$$T_f^* - T_m + \frac{T_m(c_l - c_s)}{L}\left(T_f^* \ln\frac{T_f^*}{T_m} + T_m - T_f^*\right) + \frac{\gamma(\mathbf{n})T_m}{L}\kappa + \frac{V}{\nu(\mathbf{n})} = 0, \tag{4}$$

where $\gamma(\mathbf{n})$ is the anisotropic surface tension as a function of the local surface normal orientation and κ is twice the mean interface curvature which is positive when the center of curvature lies in the solid phase. The last term accounts for the effect of anisotropic kinetic mobility, $\nu(\mathbf{n})$. It is intended to model the inherent nonequilibrium nature of the phase change process. We make the assumption that kinetic effects are linearly proportional to the interface temperature. At large undercooling and, thus, high growth velocity this parameter adds a stabilization effect to the interface by depressing the local freezing temperature. A small enough value of ν acts simply to suppress the growth of any unstable protrusions of the interface.

We note that integration of Eq. (1) across the interface directly yields the classic Stefan condition,

$$q = [k_s\nabla T_s - k_l\nabla T_l] \cdot \mathbf{n}. \tag{5}$$

Thus the formulation in Eqs. (1)–(3) satisfies the Stefan condition on the interface without the numerical difficulty of calculating temperature gradient values on the interface. Here, k_l and k_s are the liquid and solid thermal conductivities, respectively. If the heat capacity is equal in both phases and in the absence of molecular kinetic effects and anisotropy, Eq. (4) reduces to the classic Gibbs–Thomson condition:

$$T_f^* = T_m - \frac{\gamma T_m}{L}\kappa. \tag{6}$$

In order to differentiate liquid and solid material regions

we use an indicator function, $I(\mathbf{x})$, similar to the phase-field variable in phase-field models that has the value 1 in the solid phase and 0 in the liquid phase. Unlike the phase-field variable, $I(\mathbf{x})$ is constructed from the known position of the interface rather than used to determine the position of the interface. The numerical construction of the indicator function will be discussed shortly. This function allows us to evaluate the values of the material properties at every location by

$$c(\mathbf{x}) = c_l + (c_s - c_l)I(\mathbf{x}) \tag{7}$$

$$k(\mathbf{x}) = k_l + (k_s - k_l)I(\mathbf{x}). \tag{8}$$

In terms of the nondimensional temperature, volumetric heat capacity, and thermal conductivity,

$$T = \frac{c_s}{L}(T^* - T_m), \quad C = \frac{c_l}{c_s} + \left(1 - \frac{c_l}{c_s}\right) I(\mathbf{x}), \qquad K = \frac{k_l}{k_s} + \left(1 - \frac{k_l}{k_s}\right) I(\mathbf{x}), \tag{9}$$

and scaling all lengths by a suitable length scale, Z, Q, and q by c_sZ/k_sL, normal velocity by c_sZ/k_s, and time by k_s/c_sZ^2, Eqs. (1)–(4) become

$$\frac{\partial}{\partial t}(CT) = \nabla \cdot K\nabla T + Q \tag{10}$$

$$Q = \int_f q\delta(\mathbf{x} - \mathbf{x}_f)\, da \tag{11}$$

$$q = \left[1 + \left(\frac{c_l}{c_s} - 1\right) T_f\right] V \tag{12}$$

$$T_f + \left(\frac{c_l}{c_s} - 1\right) T_f^2 + \sigma_n(\mathbf{n})\kappa + \mu_n(\mathbf{n})V = 0. \tag{13}$$

The above set of nondimensional equations, Eqs. (10)–(13), is the mathematical formulation of the solidification problem which we solve numerically.

In deriving Eq. (13) we have used the first-order approximation $\ln(1 + z) \approx z$ for small z in the heat capacity term. In this case, $z = (T_f^* - T_m)/T_m$. A conservative estimate for the maximum value of z is at nucleation, where $T_f^* \approx T_\infty$. Then, maximum observed values for z are 0.14 for water, 0.04 for succinonitrile, and 0.13–0.25 for most pure metals [73], which leads to an error in the logarithm approximation of roughly 10% in the worst case and only a few percent for more typical undercoolings. Far from nucleation conditions, where our simulations are run, T_f^* is closer to T_m than it is to T_∞ and the logarithm approximation becomes even better.

In Eq. (13) the term involving the heat capacity ratio is second order in the local interface temperature, T_f, and may usually be neglected except at large undercooling. However, we note that for hypercooled situations this term is significant. In our simulations we include this term since it may have some effect in the parameter range of our simulations. We observe from Eqs. (12) and (13) that the effect of discontinuous heat capacity is governed locally by interface capillarity and kinetic effects. In general the effect should be larger for large undercooling.

The functional form of the two-dimensional anisotropic capillary parameter, $\sigma_n(\mathbf{n})$, and inverse kinetic mobility, $\mu_n(\mathbf{n})$, is similar to that used by Almgren [48],

$$\sigma_n(\theta) = \sigma[1 + A_s[\tfrac{8}{3}\sin^4(\tfrac{1}{2}m_s(\theta - \phi_s)) - 1]] \tag{14}$$

$$\mu_n(\theta) = \mu[1 + A_k[\tfrac{8}{3}\sin^4(\tfrac{1}{2}m_k(\theta - \phi_k)) - 1]] \tag{15}$$

where

$$\sigma = \frac{c_s T_m \gamma}{L^2 Z} \tag{16}$$

is the isotropic capillary parameter and

$$\mu = \frac{k_s}{\nu L Z} \tag{17}$$

is the isotropic inverse kinetic mobility. The constants A_s, A_k determine the magnitude of anisotropy, m_s and m_k determine the mode of symmetry of the crystal, and ϕ_s and ϕ_k determine the angle of the symmetry axis with respect to the x-axis. The idea behind this choice of function is to model a crystalline material with a sharp-cornered polygonal shape. For example, for $A_s = 1$, $\sigma_n(\theta)$ ranges from 0 to $\frac{8}{3}$ with a fourth-order minimum at $(\theta - \phi_s) = 2n\pi/m_s$. For $m_s = 4$ the resulting shape would be four-fold symmetric.

The numerical technique used for the simulations is based on the front tracking method developed for multifluid flows by Unverdi [74] and discussed by Unverdi and Tryggvason [75, 76] in three-dimensional simulations of rising and colliding bubbles. It has been used to study the rise of contaminated bubbles (Jan and Tryggvason [77]), the axisymmetric collision of two drops (Nobari *et al.* [78]), the thermal migration of a two-dimensional bubble cloud (Nas and Tryggvason [79]), as well as other problems. Here, we will describe the procedure as it is applied to moving boundary problems in solidification and specifically to the numerical solution of Eqs. (10)–(13).

In the numerical solution, we use a square, stationary, regular grid of mesh size h and discretize the heat equation, Eq. (10), using a conservative, second-order, centered difference scheme for the spatial variables and an explicit, first-order, forward Euler time integration method. The

method is traditionally called the forward in time, centered in space, or FTCS, scheme. (We note that the interface tracking is independent of the method used to solve the governing equations on the stationary grid and thus the method is not restricted to the use of finite differences but may be implemented using finite elements or finite volumes. Second-order time integration can also be easily implemented for increased accuracy.) We use a variable time step that depends on the mesh size, h, and the interface velocity, V. Its value is determined such that two criteria are met. First, the maximum value of the time step must satisfy the stability requirement for the two-dimensional FTCS scheme. For stability, the time step, Δt, is required to satisfy $\Delta t \leq h^2/4\alpha$, where α is the thermal diffusivity of the solid or liquid, whichever is larger. Second, we ensure that the interface does not move a distance larger than about $\frac{1}{10}$ of a mesh block in one time step. ($\frac{1}{10}$ was found to provide sufficient stability.) Thus the time step is also restricted to $\Delta t \leq h/(10|V_{\max}|)$, where $|V_{\max}|$ is the magnitude of the maximum value of the interface velocity. Generally, the first criterion determines the time step throughout most of the computation, except at early times when the interface motion is rapid.

The interface is represented by separate, nonstationary computational points connected to form a one-dimensional front which lies within the two-dimensional stationary mesh. The front is used to advect the discontinuous material property fields and to calculate interface curvature and normal velocity. The curvature, normal, and tangent at each interface point are found from a fourth-order polynomial which is fitted through each point and two adjacent points on either side of that point.

The interface deforms greatly in our simulations and it is necessary to add and delete interface points during the course of the calculation such that the distance between adjacent points, d, is maintained on the order of the stationary grid spacing, h. For our simulations we have used $0.4 < d/h < 1.6$. To accommodate topology changes, interfaces are allowed to reconnect when either parts of the same interface or parts of two separate interfaces come close together. The instantaneous change in topology is, of course, only an approximation of what happens in reality. Since it is not well known at what distance the interfaces will coalesce when brought together and we cannot resolve distances down to such a small scale, we artificially reconnect the interface when two points come closer than a small distance, p. This distance is chosen rather arbitrarily for lack of a better physical model. But here the advantage of front-tracking is evident since we can control the distance at which interfaces merge and study the effect of varying p, unlike in phase field methods where there is no active control over topology changes. While the above modifications to the interface are a major task for fully three-dimensional simulations, here the interface is simply a line and they are relatively straightforward. The interface points are connected by forward and backward linked lists and interface restructuring is simply a matter of resetting pointers.

At each time step information must be passed between the moving Lagrangian interface and the stationary Eulerian grid since the Lagrangian interface points, $\mathbf{x}_k$, do not necessarily coincide with the Eulerian grid points, $\mathbf{x}_{ij}$. This is done by a method that has become known as the *immersed boundary technique* which was introduced by Peskin [80] for the analysis of blood flow in the heart. With this technique, the infinitely thin interface is approximated by a smooth distribution function that is used to distribute the heat sources at the interface (due to liberation/absorption of latent heat) over grid points nearest the interface. In a similar manner, this function is used to interpolate the temperature field from the stationary grid to the interface. In this way, the front is given a finite thickness on the order of the mesh size to provide stability and smoothness. There is also no numerical diffusion since this thickness remains constant for all time. The interface heat sources, q_k, can be distributed to the grid and the grid temperatures, T_{ij}, can be interpolated to the interface by the discretized summations:

$$Q_{ij} = \sum_k q_k F_{ij}(\mathbf{x}_k)\Delta s_k, \tag{18}$$

$$T_k = \sum_{ij} h^2 T_{ij} F_{ij}(\mathbf{x}_k), \tag{19}$$

where Δs_k is the average of the straight line distances from the point k to the two points on either side of k. Equation (18) is the discretized form of Eq. (11), where we have approximated the Dirac function by the distribution function, F_{ij}. For $\mathbf{x}_k = (x_k, y_k)$ we have used the distribution function suggested by Peskin [81],

$$F_{ij}(\mathbf{x}_k) = \frac{f(x_k/h - i) f(y_k/h - j)}{h^2}, \tag{20}$$

where

$$f(r) = \begin{cases} f_1(r), & |r| \leq 1, \\ 1/2 - f_1(2 - |r|), & 1 < |r| < 2, \\ 0, & |r| \geq 2 \end{cases} \tag{21}$$

and

$$f_1(r) = \frac{3 - 2|r| + \sqrt{1 + 4|r| - 4r^2}}{8}. \tag{22}$$

We have also used Peskin's [80] cosine distribution function and have found no discernible difference in the results.

Tryggvason and co-workers [74–79] have extended the immersed boundary technique to accommodate discontinuous material properties through the numerical construction of an indicator function, $I(\mathbf{x})$. The jump in the indicator function across the interface is distributed to the grid points nearest to the interface using Peskin's distribution function. This generates a grid-gradient field, $\mathbf{G}(\mathbf{x})$, which is zero except near the interface, and has a finite thickness. By numerical differentiation, using second-order centered differences, we find the divergence of the gradient field, $(\nabla \cdot \mathbf{G})$, thus calculating the Laplacian of the indicator function. This is again zero, except near the interface. To find the indicator function everywhere we solve the Poisson equation

$$\nabla^2 I = \nabla \cdot \mathbf{G}. \tag{23}$$

The indicator function is constant within each material region, but it has a finite thickness transition zone around the interface and therefore approximates a two-dimensional step-function. The primary advantage of this approach is that close interfaces can interact in a natural way since the gradients simply add or cancel as the grid distribution is constructed from the information carried by the tracked front. Therefore, when two interfaces are close together the full influence of the latent heat from both interfaces is included in the heat equation. It should be noted that if the material properties are equal in both the liquid and solid regions then there is no need to construct the indicator function.

The use of front-tracking is not new to the numerical solution of solidification problems. Some features of the present method such as the interface curvature calculation and the concept of interface restructuring to maintain a fairly constant point spacing are similar to those used by Shyy [50] and Almgren [48], for example. The major novelty in the front-tracking method presented here is the use of the immersed boundary technique to transfer information between the interface and temperature grids and the construction of the indicator function which enables computations with discontinuous material properties.

In order to begin our computation we first specify an initial interface shape. From this shape we construct the indicator function as described above and determine the heat capacity and thermal conductivity fields from Eqs. (7) and (8). In a similar manner we make use of the indicator function to specify the initial temperature field,

$$T(\mathbf{x}, t = 0) = \mathrm{St}(1 + I(\mathbf{x})), \tag{24}$$

where the Stefan number, $\mathrm{St} = c_s(T_\infty - T_m)/L$, is the nondimensional undercooling. This initial temperature field is, of course, only an approximation intended to model the sudden introduction of a small seed of solid into an undercooled liquid. (The Gibbs–Thomson condition, Eq. (13), is not necessarily satisfied for the initially specified interface shape and temperature field but it is satisfied after the first time step has been taken. Since our computation utilizes a variable time step, we set the step to be initially quite small. The result after this first small time step can then be effectively considered the proper initial condition which satisfies the Gibbs–Thomson condition.)

Given the initial interface shape, temperature, and material property fields, the solution algorithm proceeds iteratively through the following steps:

1. Using an estimate for the normal velocity, V, at each interface point the heat source at the interface, q, is calculated from Eq. (12) and is distributed to the stationary grid using Eq. (18).

2. Using the velocity estimate, the interface is advected to a new position by: $V = (d\mathbf{x}_f/dt) \cdot \mathbf{n}$.

3. The indicator function is constructed from the new interface position by solving Eq. (23) and the heat capacity field is found using Eq. (7) .

4. With appropriate wall boundary conditions, Eq. (10) is solved for the temperature field at time $t + \Delta t$ by a conservative FTCS scheme.

5. This temperature field is interpolated by Eq. (19) onto the interface at its new position to find the temperature at each point on the interface.

6. If the Gibbs–Thomson condition, Eq. (13), is satisfied then the thermal conductivity field is updated to the new interface position by Eq. (8) and the computation proceeds to the next time step. Otherwise, a new estimate for V is determined and we return to step 1.

In the last step, the new estimate for V can be found by an iterative method. We have found that in one-dimensional problems, where the interface is only one point, the bisection or secant methods work successfully. In two dimensions, we must use a multidimensional iterative method since the interface now consists of many points. Here we describe a simple iteration scheme for nonlinear sets of equations which we have found to work well. In general, if the interface temperature found in step 5 is substituted into Eq. (13) the right-hand side of this equation will not equal zero but some error, $E(V)$. In order to make this error go to zero and thus satisfy Eq. (13) we use a variation of the Newton iteration method. In matrix form, the Newton iteration updates the unknown velocities at each point by the equation,

$$\mathbf{V}^{l+1} = \mathbf{V}^l - [\mathbf{J}]^{-1}\mathbf{E}^l(V^l), \tag{25}$$

where l is the iteration index, $\mathbf{V}$ and $\mathbf{E}$ are, respectively,

the $N \times 1$ column vectors of interface velocities and errors at each point. N is the number of interface points. The Jacobian, $\mathbf{J}$, is the $N \times N$ matrix of partial derivatives of the error with respect to the velocities, $J_{mn} = \partial E_m / \partial V_n$. Since these derivatives are difficult to calculate and the subsequent matrix inversion is computationally expensive, we use a different Jacobian which has the simple form

$$\mathbf{J} = a^{-1}\mathbf{I}, \tag{26}$$

where $\mathbf{I}$ is the identity matrix and a is a constant. This constant determines the rate of convergence of the iteration. In our code we adjust a manually during the first few time steps until we achieve an optimum rate of convergence. At the optimum value of a, which is different for different physical parameters, the iteration converges rather quickly to a tolerance of $\varepsilon = 10^{-5}$ in 3 to 10 iterations. The tolerance is calculated by

$$\varepsilon = \frac{1}{N}\sum_{k=1}^{N} |V_k^{l+1} - V_k^l|. \tag{27}$$

We have found that optimum values for a range roughly between 400 and 800, depending on the physical parameters.

3. RESULTS AND DISCUSSION

A. *Stable Solidification*

The two-dimensional Stefan problem of solidification in the plane due to a continuous line heat sink was solved numerically and compared with the exact analytical solution given by Carslaw and Jaeger [1] in one-dimensional axisymmetric coordinates:

$$T(r,t) = \frac{Q_L}{4\pi}\left[Ei\left(\frac{-r^2}{4t}\right) - Ei(-\lambda^2)\right] \tag{28}$$

in the solid region and

$$T(r,t) = 1 - \frac{Ei(-\alpha_s r^2/4\alpha_l t)}{Ei(-\alpha_s \lambda^2/\alpha_l)} \tag{29}$$

in the liquid region. Q_L is the strength of the line heat sink, α is thermal diffusivity, and Ei is the exponential integral. The heat source at the circular interface and its radius are

$$q(t) = \frac{\lambda}{\mathrm{St}\, t^{1/2}}, \quad R_f(t) = 2\lambda t^{1/2}, \tag{30}$$

where λ is the root of

$$Q_L = 4\pi e^{\lambda^2}\left[\frac{-k_l e^{-\alpha_s \lambda^2/\alpha_l}}{k_s Ei(-\alpha_s\lambda^2/\alpha_l)} + \frac{\lambda^2}{\mathrm{St}}\right]. \tag{31}$$

As we have noted, many researchers have performed numerical simulations of stable solidification using a variety of methods. The purpose of these computations is to demonstrate the accuracy and robustness of the front-tracking method. The problem of solidification due to a line heat sink poses an especially rigorous test of the numerical method due to the necessity of accurately predicting the location of the moving phase change interface and temperature field in the presence of large temperature gradient variations from infinity at $r = 0$ to nearly 0 at the boundary of the computational domain. In these figures we present comparisons of numerical and exact solutions for a variety of physical conditions and numerical parameters. The initial and boundary conditions on the temperature for the numerical solution correspond to the exact solution at each time step. In order to avoid computation of the infinitely negative temperature at $r = 0$, this point was placed in the center of a mesh block. The four points at the vertices of this block were maintained at the exact solution temperatures. For the stable solidification problem, we solve Eqs. (10)–(13) as described in the previous section. To be consistent with the exact solution we ignore effects due to surface tension, interface kinetics, and liquid/solid heat capacity ratio in Eqs. (12) and (13). (The effect of the heat capacity ratio is still included in Eq. (10) in the nondimensional heat capacity field, C.) Equations (12) and (13) for the stable problem become

$$q = V, \quad T_f = 0. \tag{32}$$

In Fig. 1a the average radius of all the interface points is plotted at each time for three different grid resolutions: 10×10, 20×20, and 50×50. For a heat sink strength, $Q_L = 10$, and Stefan number, $\mathrm{St} = 1$, the solution converges to the exact solution for increasing grid resolution. The numerical solution is within 0.5% of the exact solution at the 50×50 resolution. Figure 1b plots the error in radius between the exact and numerical solutions at $t = 0.15$ for several grid resolutions. For consistency, the time step was kept at the same value of $\Delta t = 3 \times 10^{-5}$ for each of the resolutions in this figure. As expected, the front tracking method exhibits between linear and quadratic convergence. Leveque and Li [82] studied elliptic equations which use Peskin's immersed boundary technique to include singular sources at an interface. They found that Peskin's method converged linearly for several simple test problems. We note that the numerical results are in good agreement with the exact solution even at low resolutions.

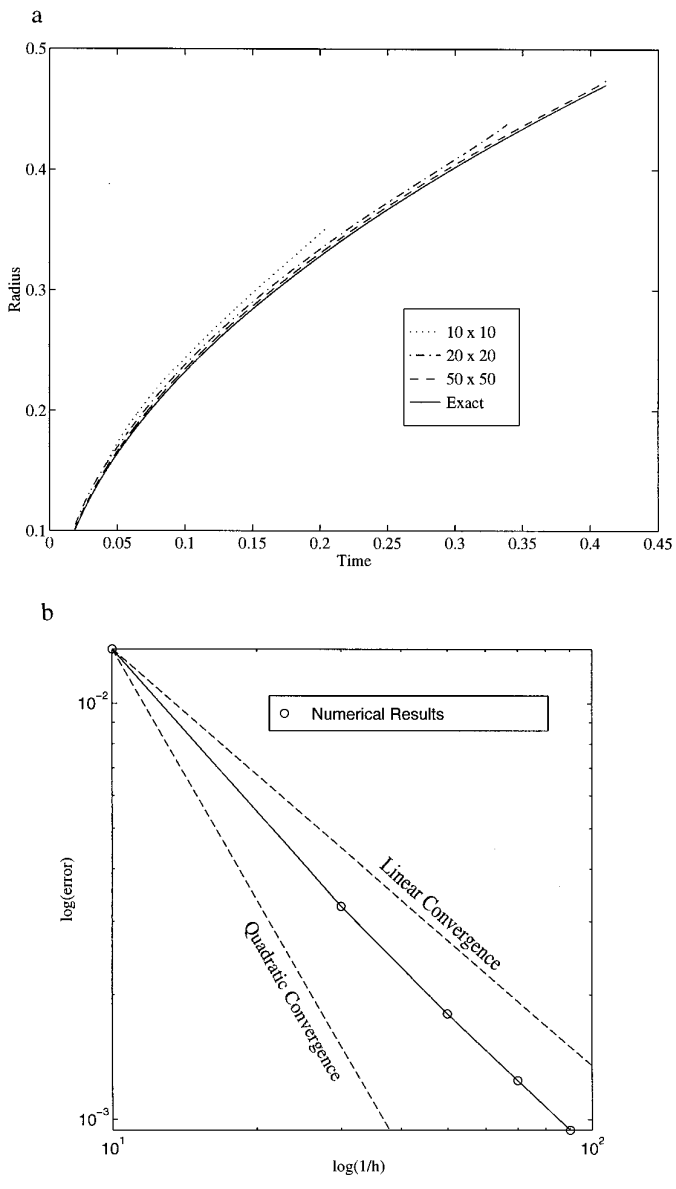

FIG. 1. Stable two-dimensional solidification by a line heat sink. A grid resolution test. In (a) the average radius of all the interface points versus time is compared to the exact solution for three different grid resolutions. In (b) the error in radius at $t = 0.15$ between the exact and numerical solutions is plotted for several grid resolutions. As expected, the front-tracking method exhibits between linear and quadratic convergence. St = 1, $Q_L = 10$, $k_l/k_s = c_l/c_s = 1$.

Thus even though the convergence is not quadratic, the constant in the error estimate is small.

The Stefan number varies with the temperature drop that the material must undergo, but for water and some nonmetals the Stefan number is typically less than unity, while for metals the Stefan number is generally 1–10. For a high Stefan number the latent heat released during solidification is small and the problem becomes essentially one

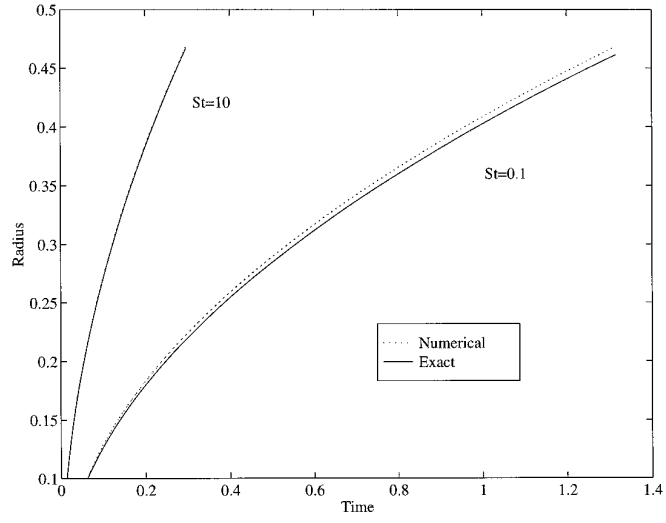

FIG. 2. Effect of varying the Stefan number, St. The average radius of all the interface points versus time is compared to the exact solution for two different Stefan numbers. 50×50 grid, $Q_L = 10$, $k_l/k_s = c_l/c_s = 1$.

of pure conduction without phase change. For a low Stefan number, the latent heat released is high and the solidification problem is dominated by conduction of the latent heat liberated at the interface. Figure 2 shows numerical and exact results for large and small Stefan numbers. A plot of average radius versus time is shown for St = 10 and St = 0.1 for a 50×50 grid resolution with a heat sink strength of $Q_L = 10$. Agreement with the exact solution is excellent for St = 10. For St = 0.1 the higher latent heat released results in a larger heat flux discontinuity at the interface. This situation is more difficult to handle numerically but the results are still within 2% of the exact solution.

In Fig. 3 the average radius versus time is plotted for two cases where the material properties in the liquid and solid phases are unequal. The results for a liquid to solid thermal conductivity ratio, $k_l/k_s = 0.2$ and a liquid to solid heat capacity ratio, $c_l/c_s = 2$, agree well with the corresponding exact solutions despite the discontinuities in the material properties. For comparison, water has $k_l/k_s \approx 0.25$ and $c_l/c_s \approx 2$. Here, St = 1, the heat sink strength is increased to $Q_L = 50$, and the grid resolution is increased to 100×100. Temperature profiles corresponding to the case where $k_l/k_s = 0.2$ are plotted along the X-axis at a one-dimensional slice through $Y = 0.51$ in Fig. 4. The four curves are plotted for increasing time from left to right at time increments of 0.02. The large temperature gradients near the line heat sink at $X = 0.505$ ($r = 0$) and the discontinuity in temperature gradient at the melting temperature, $T = 0$, due to the release of latent heat and the unequal thermal conductivities are reproduced accurately by the numerical results. The liquid/solid interfaces for the curves in Fig. 4 are plotted in Fig. 5. As the interface

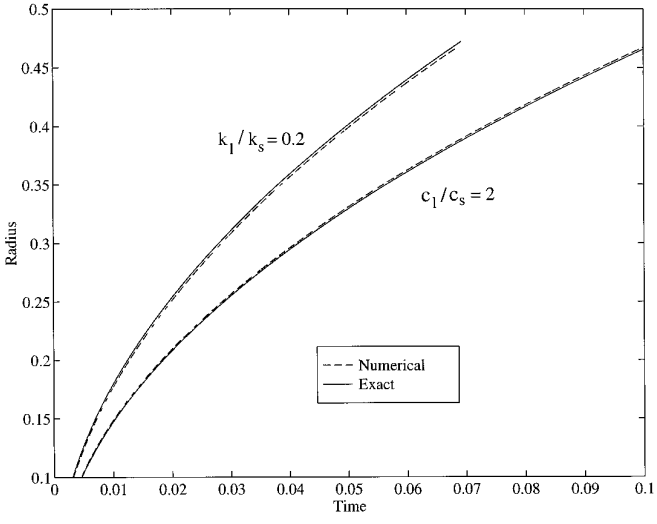

FIG. 3. Effect of varying material properties. The average radius of all the interface points versus time is compared to the exact solution for a thermal conductivity ratio $k_l/k_s = 0.2$ and a heat capacity ratio of $c_l/c_s = 2$. 100×100 grid, St = 1, $Q_L = 50$.

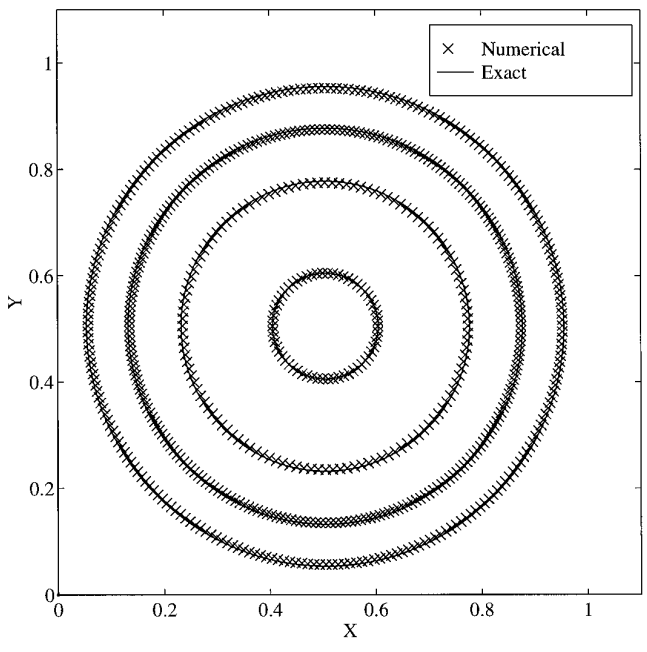

FIG. 5. Liquid/solid interfaces for the four curves in Fig. 4. As the interface expands outward in concentric circles more points are added to the interface in order to maintain an interface grid resolution on the order of a stationary grid mesh block, h. $k_l/k_s = 0.2$, $c_l/c_s = 1$, 100×100 grid, St = 1, $Q_L = 50$.

expands outward in concentric circles more points are added to the interface in order to maintain an interface grid resolution of $0.4 < d/h < 1.6$.

Figure 6 demonstrates the ability of the method to handle topology changes. In this case four heat sinks create four expanding circular regions of solid material. As these regions approach each other, their interfaces are ruptured when the distance between any interface points is less than an arbitrarily chosen proximity of $p = 0.005$. The four solid regions merge to form a large solid region with an entrapped liquid region. This four cusped liquid region circularizes and eventually disappears as it completely solidifies.

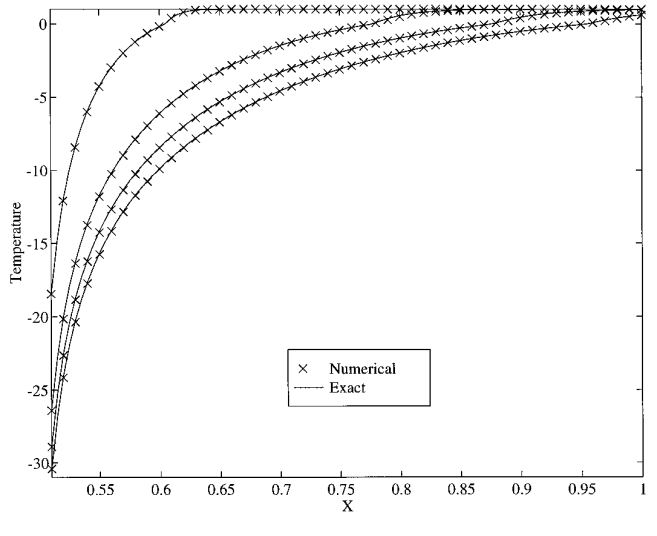

FIG. 4. Temperature profiles along the X-axis at $Y = 0.51$. The four curves are for increasing time from left to right: $t = 0.003$, 0.023, 0.043, 0.063. $k_l/k_s = 0.2$, $c_l/c_s = 1$, 100×100 grid, St = 1, $Q_L = 50$.

B. *Unstable Solidification*

We now present the results for unstable solidification into an undercooled liquid. For all of our simulations the domain boundaries are insulated. We solve the problem on the full domain and do not impose any symmetry requirements on the interface shape. The primary physical parameters are the dimensionless undercooling, St, the capillary parameter, σ, and the ratio of heat capacities and thermal conductivities in the solid and liquid regions. The process of solidification into an undercooled liquid is inherently unstable and sensitive to initial conditions. The degree of instability in the growing solid depends on the choice of physical parameters. Typically, for high σ and low St the liquid/solid interface remains smooth for long periods of growth while for low σ and high St the interface deforms quickly into a branching dendritic pattern. In our results we look at the effects of different physical and numerical parameters on the time-evolving interface shapes, as well as on global quantities of interest such as solid fraction and total interface length.

Figure 7 shows results for four different grid resolutions.

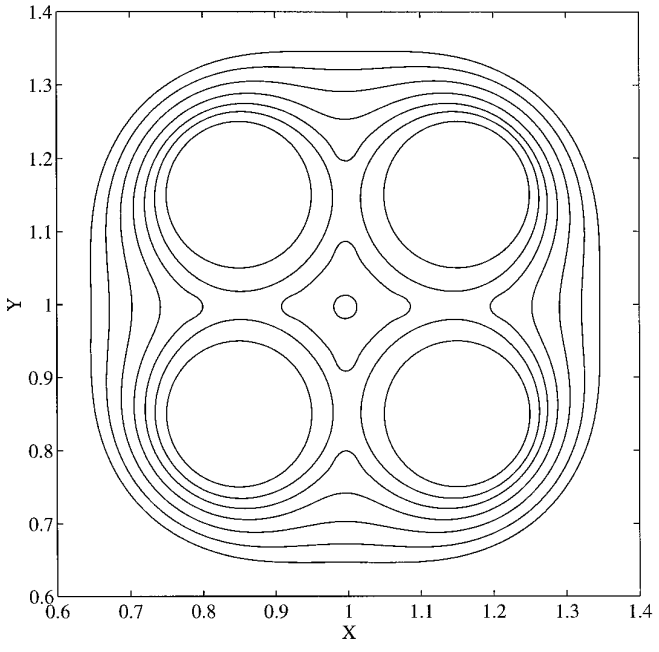

FIG. 6. Topology change. Four heat sinks create four expanding regions of solid. As the solidifying regions approach each other their interfaces are ruptured when the distance between any interface points is less than $p = 0.005$. The four solid regions merge to form a large solid region with an entrapped liquid region in the center. This four cusped liquid region circularizes and eventually disappears as it completely solidifies. The physical domain is 2×2, 100×100 grid, St $= 1$, and $k_l/k_s = c_l/c_s = 1$.

For these cases St $= -0.5$, $\sigma = 0.002$, and $\mu = 0.002$ with no anisotropy ($A_s = A_k = 0$) and equal material properties in the liquid and solid. Interface points are added or deleted as required to maintain a point spacing of $0.4 < d/h < 1.6$. The computational domain is a square with sides of length 4. The shape of the initial interface is specified by

$$x_f = x_c + R\cos(\theta), \quad y_f = y_c + R\sin(\theta), \tag{33}$$

where θ is measured counterclockwise from the x-axis and

$$R = R_o + R_b\cos[M(\theta + \theta_o)]. \tag{34}$$

In this figure, the choice $(x_c, y_c) = (2, 2)$, $R_o = 0.1$, $R_b = 0.02$, $M = 4$, and $\theta_o = 0$ produces a perturbed circle with four lobes aligned with the coordinate axes. The time-evolving interfaces are plotted for all four grid resolutions at equal nondimensional time increments of 0.03. The final interface plotted for the 100×100 mesh contains 1345 interface points and is at time 0.09. The 200×200 mesh contains 1746 points and is at time 0.63. For the 300×300 mesh the last shape contains 2053 points at time 0.81 and for 400×400, 2542 points also at time 0.81. We note that these results show the effect of time as well as grid resolution since the maximum time step decreases with grid resolution. Figure 8 shows plots of various interface quantities for the increasing grid resolutions shown in Fig. 7. Plotted versus time are the fraction of material solidified, the total interface length, and the maximum radius (maximum distance of an interface point from the center of the initial interface, $(x_c, y_c) = (2, 2)$).

The grid resolution obviously has considerable effect on the solution. For the lowest resolution, the interface branches excessively, and a comparison with the results on the finer grids shows that the solution is dominated by grid effects. The solution of the finer grids, on the other hand, all have essentially the same features. The four initial protrusions, or fingers, grow and become wider and then split. The eight resulting fingers also become wider as they grow and eventually split. The difference between the solutions on the three grids is the time when the fingers split. On the coarsest grid (200×200) the splitting takes place early and we have sixteen well developed fingers at the final time. As the grid is made finer, the fingers split later, although the difference between the 300×300 grid and the 400×400 grid is relatively small. The results are very much as we should expect. The fingers split due to secondary instabilities and these depend sensitively on the amount of noise present. Generally, we expect larger perturbations on the coarser grid and an earlier onset of instability. Therefore, while the solutions in Figs. 7 and 8 are not fully converged in the sense that the two finest grids give completely identical solutions, we believe that the physical phenomena are fully resolved for both grids. Or, said differently, the important distinction between the solution on the 100×100 grid and the three finer grids is that the instabilities on the 100×100 grid are completely artificially created by the grid noise while on the finer resolutions the grid noise only acts to trigger the onset of the physical Mullins–Sekerka instability. As the resolution increases and the noise decreases, this physical instability is triggered at later times. In a physical situation, the Mullins–Sekerka instability would be similarly triggered by thermal fluctuations due to fluid convection or random statistical fluctuations. In most cases, we want to trigger these instabilities anyway, so perturbations induced by the grid are not necessarily undesirable. If we wished to eliminate the grid effect completely, we could, of course, introduce noise explicitly at a sufficiently high level to swamp the grid noise.

A consequence of the earlier tip splitting (and smaller tip radii) produced on coarser grids is an increase in tip growth speed. The increased growth speeds at lower grid resolutions is evident in Fig. 8, particularly in the plot of maximum radius versus time. This trend of increased tip speed with the decrease in tip radius is an expected result. Indeed, the trend is similar to Ivantsov's simplified analysis of a growing dendrite [18]. There he found an inverse

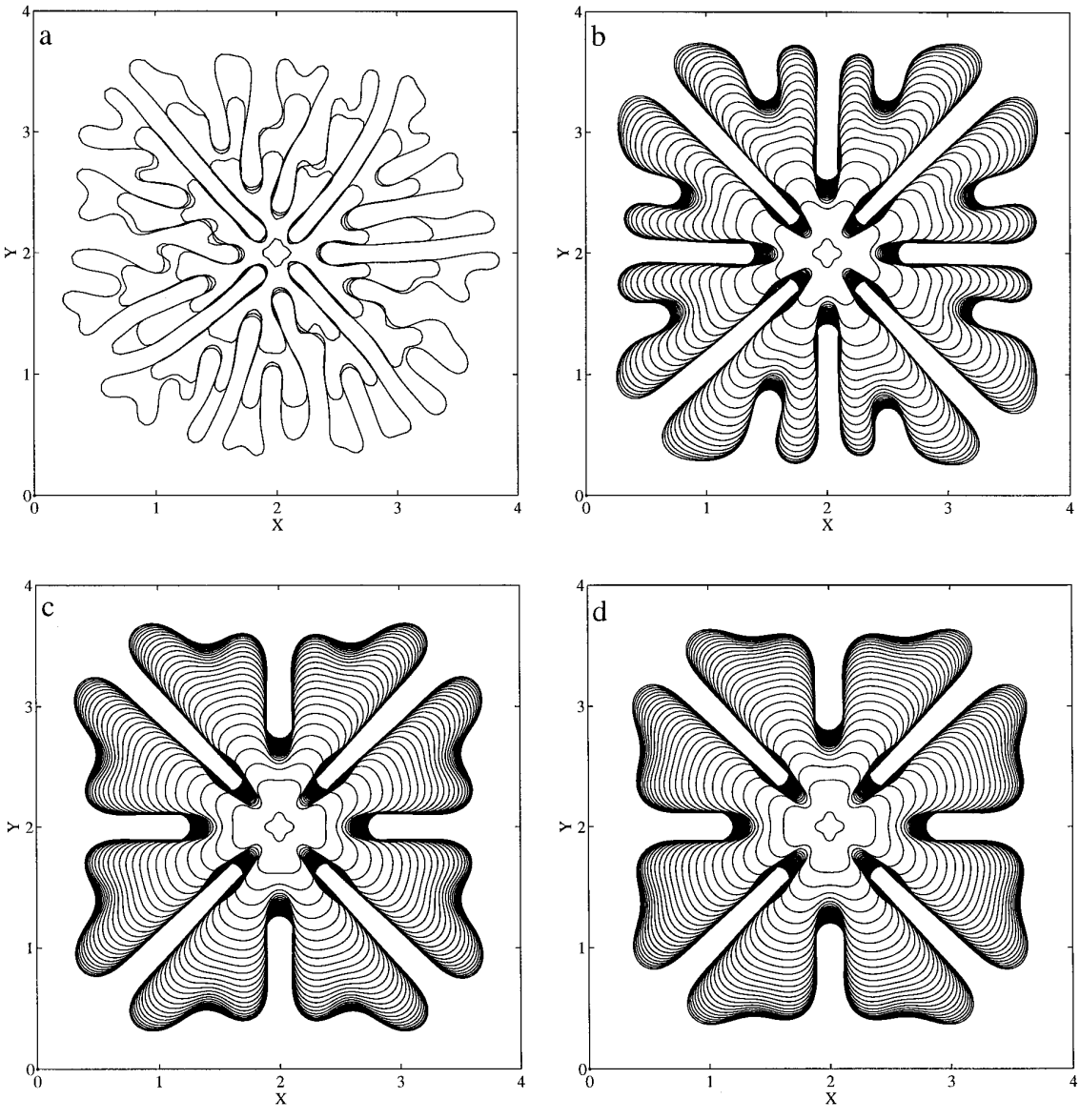

FIG. 7. A grid resolution study for dendritic solidification in an insulated cavity. The interface evolution for four grid resolutions is plotted at equal nondimensional time increments of 0.03. As the grid resolution increases the interface shapes become more symmetric and grid independent. The results reproduce the classic tip splitting instability of dendritic solidification. The final interface plotted for the 100×100 mesh in (a) contains 1345 interface points at time 0.09. The last interface for the 200×200 mesh in (b) contains 1746 points and is at time 0.63. For the 300×300 mesh in (c) the last shape contains 2053 points at time 0.81 and for the 400×400 mesh in (d), 2542 points also at time 0.81. St $= -0.5$, $\sigma = 0.002$, $\mu = 0.002$ with no anisotropy ($A_s = A_k = 0$) and equal material properties ($c_l/c_s = k_l/k_s = 1$).

relationship between dendrite tip speed, V, and tip radius, R, namely, $VR =$const.

Although we do not show the results here, we have also studied the influence of interface point spacing, d. We have run the same computations as shown in Fig. 7 with interface point spacings of $0.2 < d/h < 0.8$ and $0.8 < d/h < 3.2$. For the three higher grid resolutions, the effect on the interface shape, as well as the solid fraction, interface length, and maximum radius, is negligible. The results appear to be independent of the interface point spacing for a reasonable choice of point spacings. This also indicates that the interface curvature calculation using a simple fourth-order polynomial curve fit is sufficiently accurate. All of the remaining computations shown here have a point spacing of $0.4 < d/h < 1.6$.

To demonstrate that the solution is independent of grid orientation, we compared runs with different initial interface rotations, θ_o. The interface in Fig. 7d with $\theta_o = 0$ was

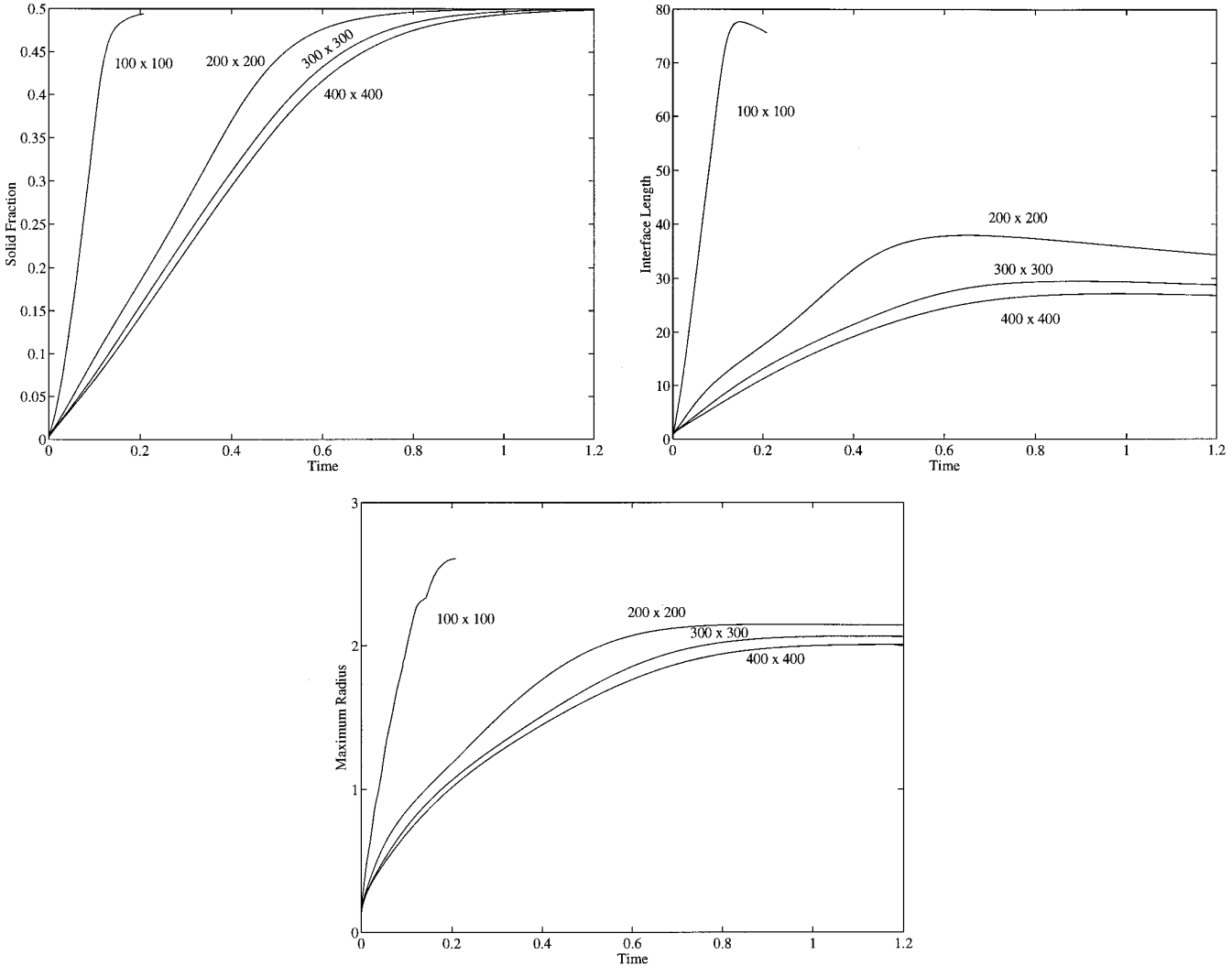

FIG. 8. The solid fraction, total interface length, and maximum radius versus time are plotted for the various grid resolutions corresponding to the interface plots in Fig. 7. The solid fraction, interface length, and maximum radius demonstrate better than linear convergence with increasing grid resolution. St $= -0.5$, $\sigma = 0.002$, $\mu = 0.002$ with no anisotropy ($A_s = A_k = 0$) and equal material properties ($c_l/c_s = k_l/k_s = 1$).

compared to two runs with $\theta_o = 27$ and $\theta_o = 45$. The interface shapes from the two runs at $t = 0.21$ were then rotated back 27° and 45° respectively and plotted over each other for comparison. The three interfaces were nearly indistinguishable from one another. A plot of this result would look identical to the interface in Fig. 7d at $t = 0.21$ and thus is not included here.

In Fig. 9a an initially fivefold symmetric interface ($M = 5$) maintains its symmetry throughout the computation. The last interface shown contains 2113 points at $t = 0.42$. Other than $M = 5$, the parameters for this run are the same as in Fig. 7d. Clearly there is no grid induced anisotropy and the alignment of the tracked front with the underlying stationary grid does not affect the solution. A plot of the interface curvature as a function of the surface distance in Fig. 9b demonstrates the fivefold symmetric structure. This plot corresponds to the last interface in Fig. 9a. The interface curvatures for each of the five main branches in Fig. 9a are plotted over each other. The curvature repeats nearly identically five times around the interface. The slight discrepancies in curvature from one branch to another may be partly attributed to the effect of the domain boundaries. The smoothness of the curvature plot again suggests that the simple fourth-order curve fit we have used is sufficiently accurate in calculating interface curvature.

The condition for homogeneous nucleation of a small

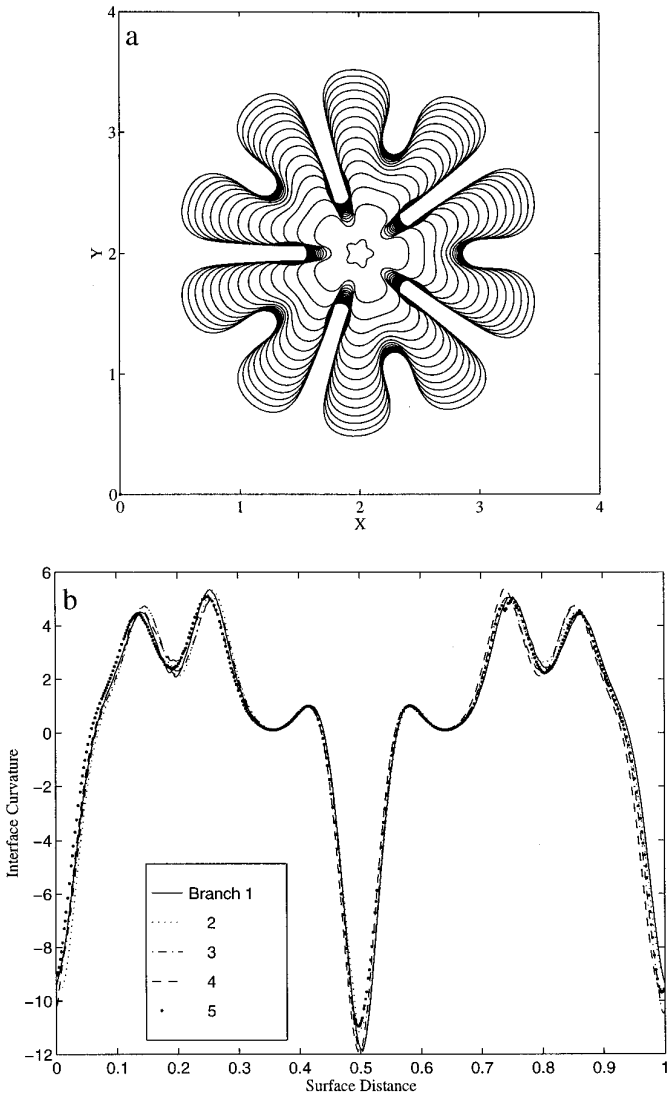

FIG. 9. At the top an initially fivefold symmetric interface ($M = 5$) maintains its symmetry throughout the computation. The last interface shown contains 2113 points at $t = 0.42$. There is no grid induced anisotropy. Below, a plot of the interface curvature as a function of the surface distance for the last interface in (a) shows that the curvature repeats nearly identically five times around the interface. The interface curvatures for each of the five main branches in (a) are plotted over each other. $M = 5$, St $= -0.5$, $\sigma = 0.002$, $\mu = 0.002$, $A_s = A_k = 0$, $c_l/c_s = k_l/k_s = 1$, and a 400×400 grid.

spherical nucleus is that the total excess free energy, ΔG, of the nucleus is maximum. The excess free energy has volume and surface contributions:

$$\Delta G = -\frac{4}{3}\pi r^3 \frac{L}{T_m}\Delta T + 4\pi r^2 \gamma. \tag{35}$$

This leads to the concept of a critical nucleation radius above which a solidifying particle will grow and below which it will collapse. In a two-dimensional system this critical radius is

$$R^* = -\frac{\sigma}{\mathrm{St}}. \tag{36}$$

In order to see if we could simulate this critical radius we performed three calculations, all with $\sigma = -\mathrm{St} = 0.5$ and thus a theoretical critical radius of $R^* = 1$. The initial interface for the first case is a circle of radius 1.01, slightly larger than the critical radius. The second case started with a circle of radius 1 and the third with a radius of 0.99. Figure 10 plots the average radius versus time for all three interfaces. The circle of initial radius 1.01 grows, that with an initial radius of 0.99 collapses. The circle that started at the critical radius $R^* = 1$ stays at 1. As predicted, our simulations show that a nucleus below the critical radius will not grow, whereas a nucleus above the critical radius does grow. For these simulations we used equal material properties in the liquid and the solid, isotropic surface tension, and no kinetic effects, $\mu = 0$. The grid resolution was 300×300 in a 10×10 square domain.

We next investigate the effect of discontinuous thermal conductivity and heat capacity between liquid and solid phases. The results for the interface evolution for various

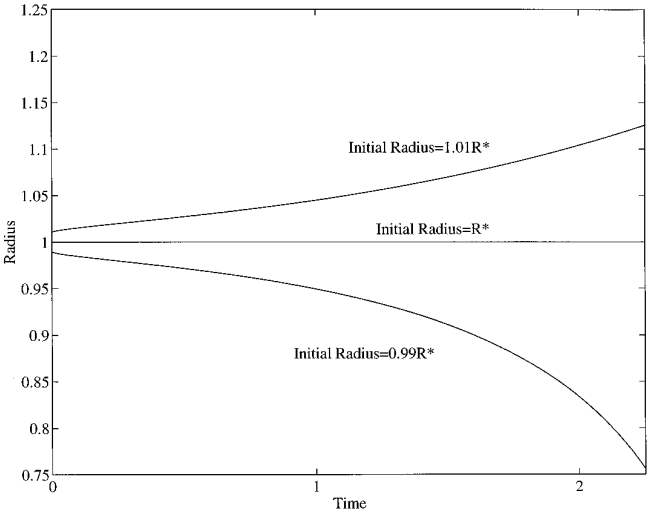

FIG. 10. Simulation of the critical nucleation radius. In a two-dimensional system the critical nucleation radius is $R^* = -\sigma/\mathrm{St}$. Here, $\sigma = -\mathrm{St} = 0.5$ and thus the critical radius is $R^* = 1$. The radius versus time for three different initial radii is shown. A circle of initial radius 1.01 grows; one with initial radius of 0.99 collapses. A circle started at the critical radius $R^* = 1$ stays at 1. As predicted, our simulations show that a nucleus below the critical radius will not grow, whereas a nucleus above the critical radius does grow. $\mu = 0$, no anisotropy ($A_s = A_k = 0$), and $c_l/c_s = k_l/k_s = 1$. The grid resolution is 300×300 in a 10×10 square domain.

thermal conductivity and heat capacity ratios are shown in Figs. 11 and 12. (Figures 11b and 12b are the same as Fig. 7c and are shown again here to facilitate comparisons.) The parameters for these cases are the same as in Fig. 7c, except that the material property ratios are varied. Again, the interfaces are plotted at equal nondimensional time increments of 0.03.

Figure 11 shows the effect of increasing k_l/k_s with $c_l/c_s = 1$. Increasing the thermal conductivity ratio primarily affects the growth rate of the solid and has little effect on the shape or stability of the interface. The relationship between the interface velocity and the thermal conductivity ratio becomes apparent when we look at the nondimensional form of the Stefan condition, Eq. (5). At the interface

$$q = V = \left[\nabla T_s - \frac{k_l}{k_s} \nabla T_l \right] \cdot \mathbf{n}. \tag{37}$$

Compared to the temperature gradient on the liquid side of the interface, the temperature gradient on the solid side remains small throughout the computation since both the interface temperature and the temperature in the bulk of the solid remain near the equilibrium freezing temperature. If we neglect the temperature gradient in the solid, then the interface velocity is proportional to the thermal conductivity ratio. The results in Figs. 11a–c are consistent with this analysis. As the liquid to solid thermal conductivity ratio increases from $k_l/k_s = 0.2$ to 2, a tenfold increase, the growth rate of the solid increases roughly threefold. A comparison with the exact solution of the problem of stable solidification by a line heat sink discussed earlier shows that in the stable case the magnitude of the growth rate roughly doubles with the same tenfold increase in k_l/k_s. (The trend of increased growth rate with increased k_l/k_s is reversed for the problem of stable solidification. This is due to the fact that the liquid is not undercooled and the temperature gradients in the liquid and solid regions are both positive.)

Figure 12 shows the effect of increasing c_l/c_s with $k_l/k_s = 1$. Increasing the heat capacity ratio even slightly has a dramatic effect on the interface stability as well as the growth rate. The effect is much more pronounced than it is for a change in the thermal conductivity ratio discussed above. A higher liquid to solid heat capacity ratio produces a fast growing unstable solid while a low ratio produces a slow growing more stable solid shape. In going from $c_l/c_s = 0.83$ to 1.2 the growth rate nearly doubles. In comparison with the problem of stable solidification by a line heat sink, such a large change in growth rate with a small change in c_l/c_s is not expected. The exact solution for the stable problem shows only a 10% change in the magnitude of the solid growth rate for the same change in c_l/c_s. (Again, the trend of increased growth rate with increased c_l/c_s is reversed for the problem of stable solidification due to the fact that the liquid is not undercooled and the temperature gradients in the liquid and solid regions are both positive.)

There appear to be two mechanisms related to the heat capacity ratio which explain these effects. The first mechanism is simply a manifestation of elementary unsteady heat conduction and does not take interface curvature into account. The overall increase in growth rate with increased heat capacity ratio is a direct result of the varying ability of materials with different heat capacities to adjust to thermal changes. A material with a low volumetric heat capacity will respond quickly to thermal changes while one with a high heat capacity will respond slowly. Therefore, a liquid with a high heat capacity has less of an ability to diffuse the latent heat released in a given time. This results in a steeper temperature gradient in the liquid adjacent to the interface. According to the Stefan condition, Eq. (37), a larger liquid side temperature gradient results in a higher interface velocity. Furthermore, interface movement in the direction of the liquid steepens the liquid side temperature gradient even more. Conversely, a lower interface velocity would result from a lower liquid phase heat capacity. The second mechanism produces an increase in interface instability with increased c_l/c_s and can be explained by Eqs. (12) and (13). If we neglect the second-order temperature term, anisotropy, and interface kinetics in Eq. (13) and combine the two equations to eliminate T_f then we can write Eq. (37) as

$$q = \left[1 - \left(\frac{c_l}{c_s} - 1 \right) \sigma \kappa \right] V = [\nabla T_s - \nabla T_l] \cdot \mathbf{n}. \tag{38}$$

The coefficient of the local normal interface velocity, V, depends on the heat capacity ratio and the local interface curvature. If $c_l/c_s > 1$ then in regions of positive curvature, where the interface grows the fastest, this coefficient is less than 1. For a given q, V must increase to compensate for the low coefficient. In regions of negative curvature, the coefficient of V is greater than 1 and thus V is lower for the same q. The net result is an increase in interface instability. Regions of the interface where the interface curvature is positive grow faster and regions of the interface where the curvature is negative slow down. The opposite occurs if $c_l/c_s < 1$. In regions of positive curvature, the coefficient of V is greater than 1. For the same q, V must be lower. In regions of negative curvature, the coefficient of V is less than 1 and thus V is higher for the same q. The net result is a more stable interface where positive curvature regions grow relatively slowly and negative curvature regions grow relatively rapidly. Furthermore, the two mechanisms described above are coupled in the sense that the local instabilities produced by the second mechanism are enhanced by the global velocity changes in the first.

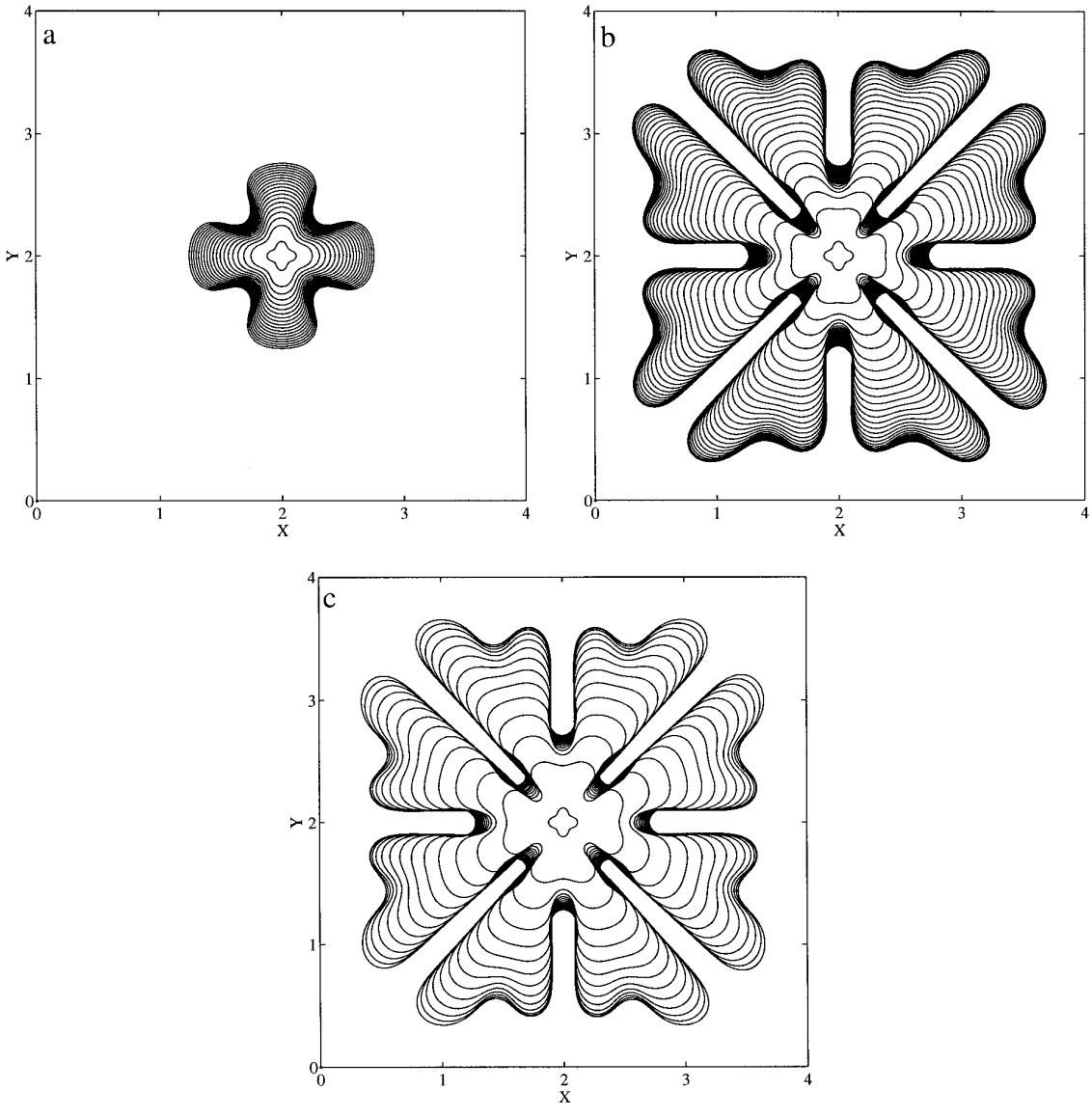

FIG. 11. The effect of varying the liquid to solid thermal conductivity ratio. The interfaces are plotted at equal time increments of 0.03. (Here, Fig. 11b is the same as Fig. 7c.) Increasing the thermal conductivity ratio increases the growth rate of the solid but has little effect on the interface shape or stability. St $= -0.5$, $\sigma = 0.002$, $\mu = 0.002$ with no anisotropy ($A_s = A_k = 0$), $c_l/c_s = 1$, and a 300×300 grid. In Fig. 11a $k_l/k_s = 0.2$. In Fig. 11b $k_l/k_s = 1.0$. In Fig. 11c, $k_l/k_s = 2.0$.

The above argument and the results in Fig. 12 suggest that discontinuity of heat capacity is a crucial consideration when modeling solid growth rates and interface morphology in the dendritic freezing of water, ($c_l/c_s \approx 2$), and some metals such as lead ($c_l/c_s \approx 1.1$), copper and nickel ($c_l/c_s \approx 1.05$), and molybdenum ($c_l/c_s \approx 1.7$) [83]. Most common pure metals have $c_l/c_s \geq 1$ and thus tend toward more instability. However, it would be difficult to experimentally isolate the effect of discontinuous heat capacity, for example, on different materials. Other physical parameters such as surface tension would usually vary along with the heat capacity ratio.

The strong interface branching exhibited in Figs. 12c, d may indicate that these results are not completely converged. However, the results of a resolution study show about the same rate of convergence as in Fig. 7. As the grid resolution is increased the interfaces become more symmetric and the interface growth rate is slightly lower. However, the primary trends of increased interface velocity and instability remain and are due to the increase in c_l/c_s.

A plot of a solid fraction versus time in Fig. 13 clearly shows the increase in growth rate with increased c_l/c_s. Also plotted as dashed lines are the maximum theoretical solid

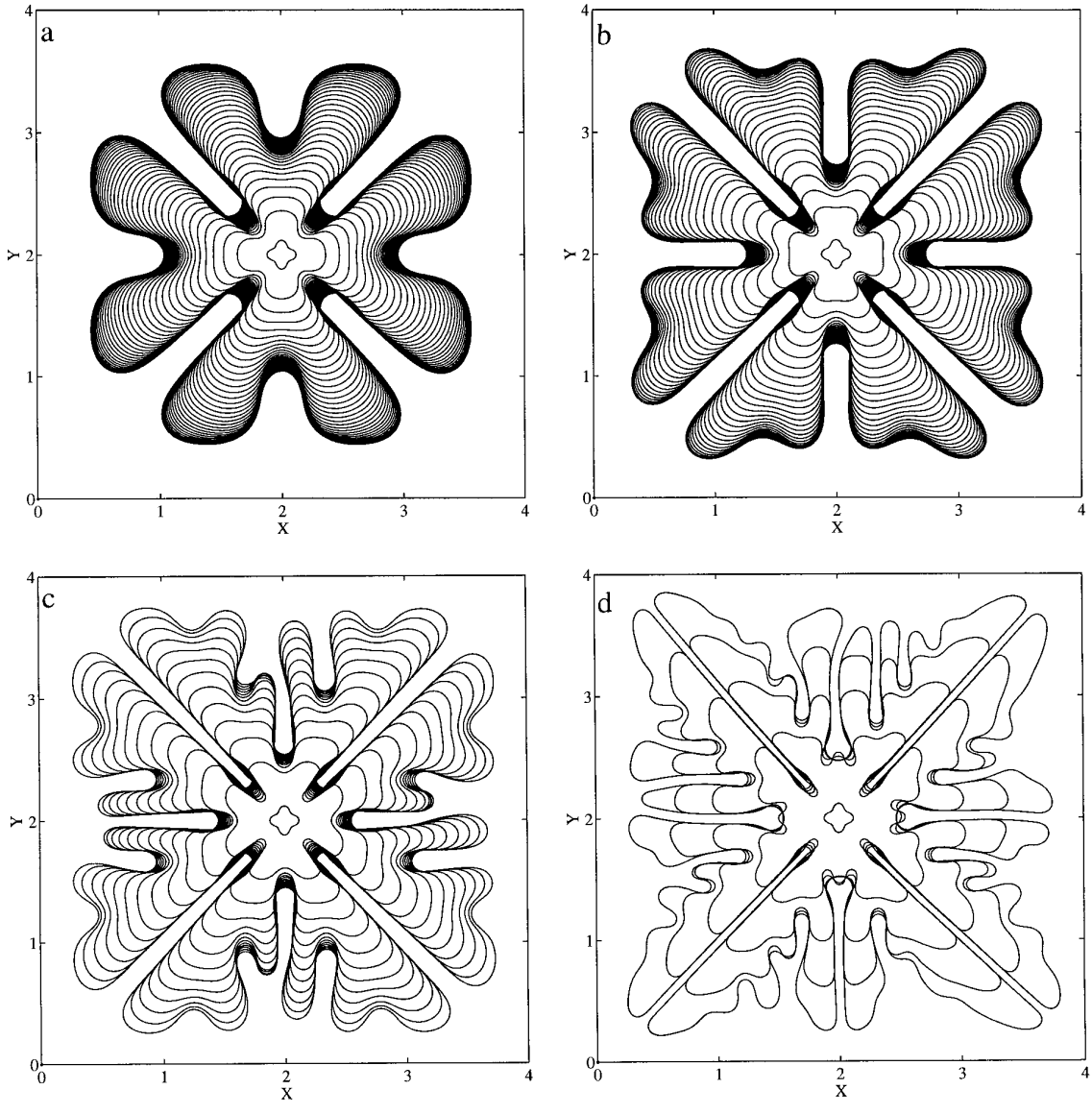

FIG. 12. Effect of varying the liquid to solid heat capacity ratio. The interfaces are plotted at equal time increments of 0.03. (Here, Fig. 12b is the same as Fig. 7c.) Increasing the heat capacity ratio increases the instability of the interface as well as the growth rate. St $= -0.5$, $\sigma = 0.002$, $\mu = 0.002$ with no anisotropy ($A_s = A_k = 0$), $k_l/k_s = 1$, and a 300×300 grid. In 12a $c_l/c_s = 0.8\overline{3}$. In 12b $c_l/c_s = 1.0$. In 12c $c_l/c_s = 1.2$; in 12d $c_l/c_s = 1.4$.

fractions for the various heat capacity ratios. The maximum theoretical amount of solid that can be formed from an undercooled liquid in an insulated cavity can be found from simple energy conservation to be

$$f_s = -\frac{c_l}{c_s}\,\mathrm{St} \tag{39}$$

which states that the only source of energy available to raise the temperature of the liquid to the equilibrium melting temperature comes from the latent heat released at the interface. The numerically calculated value of the solid fraction at large time agrees well with the theoretical limit but begins to differ slightly at higher c_l/c_s. This discrepancy is due to the higher interface curvatures at higher c_l/c_s. At high curvatures, interface temperatures deviate from the equilibrium freezing temperature because of capillary effects (the Gibbs–Thomson condition). Equation (39) does not take these capillary effects on the temperature into account.

In Fig. 14 we see the effect of a sixfold anisotropy ($m_s = 6$) in the surface tension. The interfaces are plotted at equal increments of $t = 0.003$ and the last interface shown is at $t = 0.03$ with 5854 points. The anisotropy

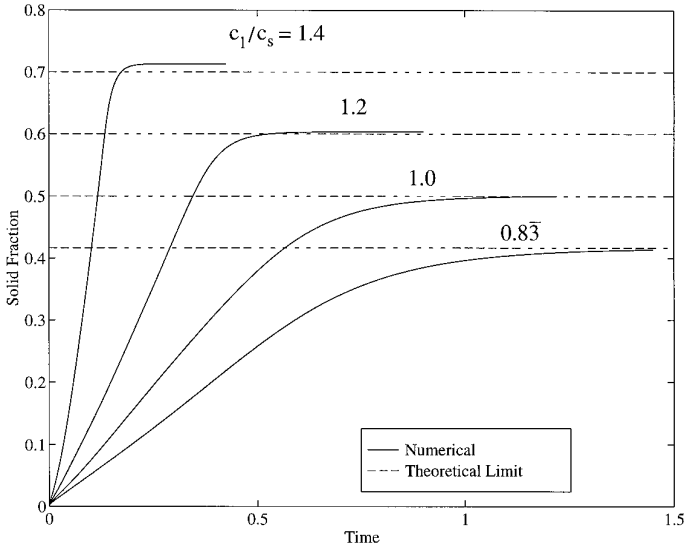

FIG. 13. The solid fraction versus time shows the increase in growth rate of the solid with increasing c_l/c_s. Also plotted are the maximum theoretical solid fractions for the various heat capacity ratios. The numerically calculated values of the solid fraction at large time agree well with the theoretical limits but begin to differ slightly at higher c_l/c_s. This discrepancy is due to capillary effects on the temperature which are not taken into account in the theoretical solid fraction. St $= -0.5$, $\sigma = 0.002$, $\mu = 0.002$ with no anisotropy ($A_s = A_k = 0$), and a 300×300 grid.

strength, A_s, is 0.4 and the other parameters remain the same as in Fig. 7d. The initial four-lobed interface no longer imparts a fourfold symmetry to the evolving interface as it did with the isotropic simulations. Growth occurs along six primary directions dictated by the surface tension anisotropy. The undercooling has a high value of St $= -0.8$ which produces a more complex shape with smaller features. In order to spatially resolve this computation we need to be able to resolve the smallest features with at least as many mesh points as were required by the smallest features in Fig. 7d. The smallest features of Fig. 7d are approximately 0.08 across and are resolved on a 400×400 grid. The smallest features in Fig. 14 are the developing side branches which are about 0.06 across and thus should be resolved on the 800×800 grid used here. The six primary dendrite arms are certainly fully resolved at this scale. Although the major structures grow symmetrically, the small side branch disturbances emanating from the primary arms begin to grow asymmetrically. Murray *et al.* [68] have found in their phase field computations that the production of side branches was very sensitive to noise, whereas the main dendrite tips were insensitive to noise. Figure (14) agrees with this assessment. The main branches grow symmetrically with a constant speed, after the initial transient, of $V = 40$ (see Fig. 16) and tip curvature of approximately $\kappa = 60$, whereas the side branches develop asymmetrically and are sensitive to small numerical inaccuracies and grid noise. Once the symmetry is broken, however slightly, the competition between neighboring side branches results in the growth of some branches and melting back of others.

A relation for the shortest wavelength at which a disturbance on a planar interface, moving with velocity V, becomes unstable is given by Mullins and Sekerka [13]:

$$\lambda_s \sim \sqrt{\sigma/V}. \tag{40}$$

Although the interface in our simulations is not planar, we can assume the same relationship approximately holds. It is clear that the problem of resolving the shorter unstable wavelengths at low σ or high undercooling and thus high V, limits all grid based numerical simulations.

In Fig. 15, a more developed side branch structure results from lower surface tension. The parameters here are the same as in Fig. 14, except the capillary parameter is reduced to $\sigma = 0.001$. The initial temperature field for this computation is a uniform temperature given by $T(\mathbf{x}, t = 0) = \mathrm{St}$ and not by Eq. (24) as in the previous runs. The interfaces are plotted at equal increments of $t = 0.003$ and the last interface shown is at $t = 0.021$ with 11,002 points. With σ reduced by half, the primary dendrite arms grow with a

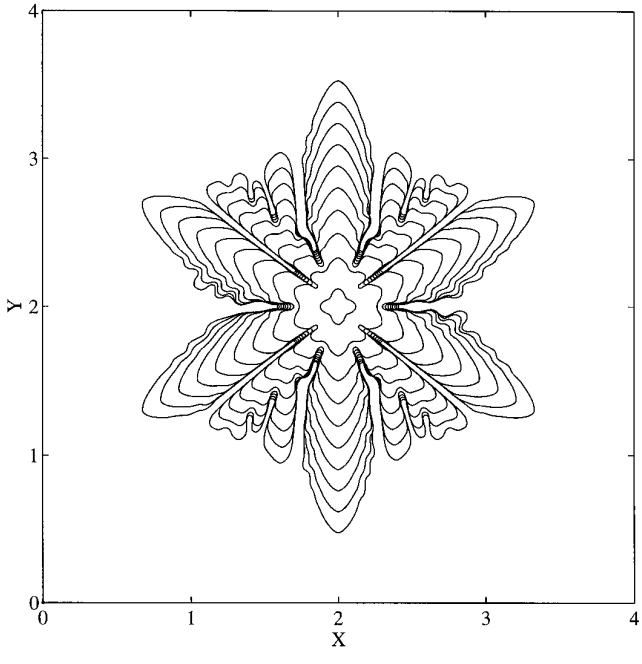

FIG. 14. With sixfold anisotropy ($m_s = 6$) in the surface tension, growth occurs along six primary directions. The interfaces are plotted at equal increments of $t = 0.003$ and the last interface shown is at $t = 0.03$ with 5854 points. The undercooling has a high value of St $= -0.8$ which produces a more complex shape with smaller features. 800×800 grid, $\sigma = 0.002$, $A_s = 0.4$ $\mu = 0.002$, $A_k = 0$ with equal material properties ($c_l/c_s = k_l/k_s = 1$).

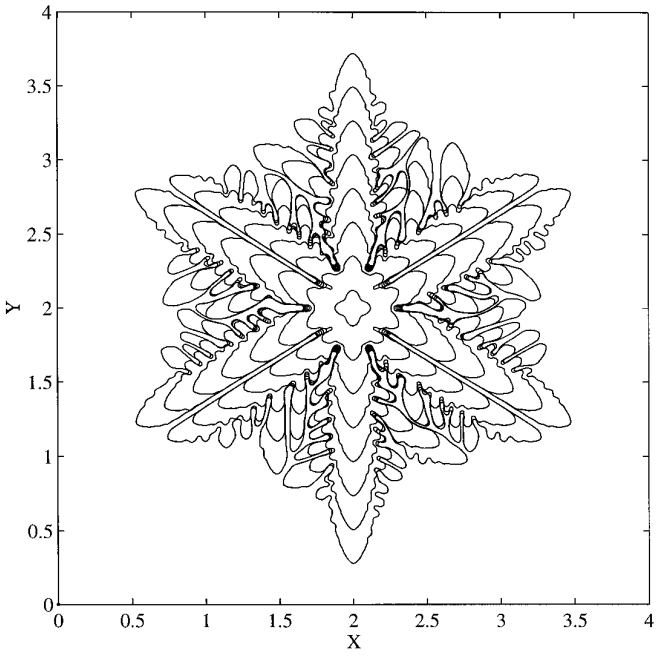

FIG. 15. A more well-developed side branch structure results from lower surface tension. The parameters here are the same as in Fig. 14 except the capillary parameter is reduced to $\sigma = 0.001$. The interfaces are plotted at equal increments of $t = 0.003$ and the last interface shown is at $t = 0.021$ with 11,002 points. 800×800 grid, $\sigma = 0.001$, $A_s = 0.4$ $\mu = 0.002$, $A_k = 0$ with equal material properties ($c_l/c_s = k_l/k_s = 1$).

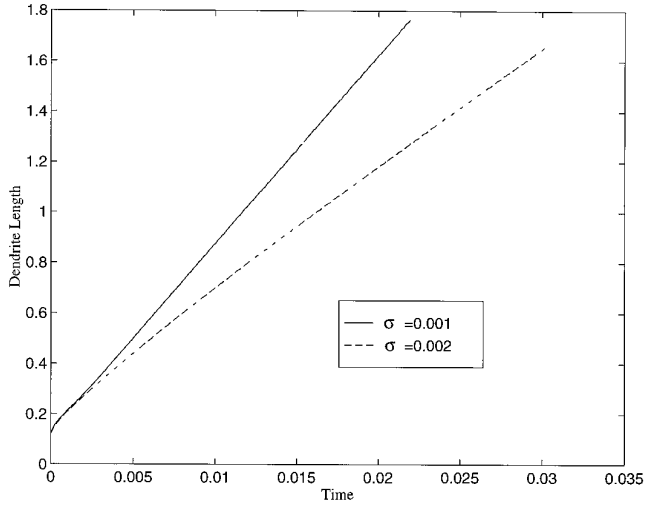

FIG. 16. A plot of the dendrite length (length of the primary dendrite arm in the first quadrant) versus time. For the two cases in Figs. 14 and 15. The slopes are constant throughout most of the computation which indicates that the dendrite tip speed, V, is constant. For $\sigma = 0.001$, V is approximately 60 while for a higher surface tension, $\sigma = 0.002$, the tip speed drops to approximately 40.

larger but still constant speed of $V = 60$ (see Fig. 16) and a higher tip curvature of approximately $\kappa = 100$. Consistent with Eq. (40), the shortest wavelength of the side branch instabilities in Fig. 15 is roughly $\frac{3}{5}$ of what it is in Fig. 14. With these smaller features we are reaching the limit of spatial resolution for the 800×800 grid used here. The competition between neighboring side branches is more intense in this figure and results in an earlier onset of asymmetry.

For the two cases in Figs. 14 and 15, Fig. 16 plots the dendrite length (length of the primary dendrite arm in the first quadrant) versus time. The slopes are constant throughout most of the computation which indicates that the dendrite tip speed, V, is constant. For $\sigma = 0.001$, V is approximately 60 while for a higher surface tension, $\sigma = 0.002$, the tip speed drops to approximately 40.

Figure 17 demonstrates the ability of the front-tracking method to easily handle qualitatively realistic topology changes. The interfaces are allowed to merge and form islands of trapped liquid. The parameters for this case are the same as in Fig. 15. Interfaces are merged and reconnected when the distance between any two points is less than $p = 0.013$. The interface consists of 11 surfaces, 10,890 points, and is plotted at $t = 0.021$. Here, the phenomena of liquid trapping and coarsening are reproduced. Sev-

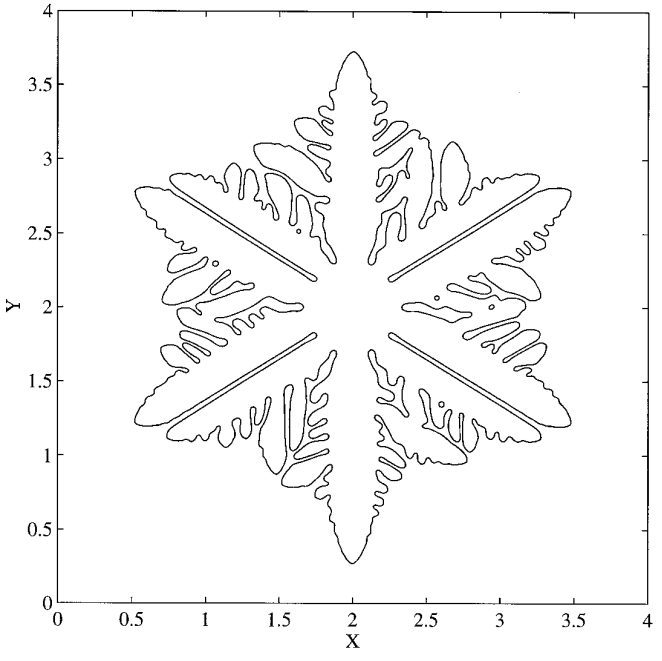

FIG. 17. Demonstration of topology change with sixfold anisotropy ($m_s = 6$) in the surface tension. Interfaces are merged when the distance between any two points is less than $p = 0.013$. The interface consists of 11 surfaces, 10,890 points, and is plotted at $t = 0.021$. The qualitatively realistic phenomena of liquid trapping and coarsening are reproduced. Several of the liquid islands have become circularized due to the effect of surface tension. The smaller islands eventually completely solidify. The parameters for this case are the same as in Fig. 15. Comparison between this figure and Fig. 15 shows that, other than the topological changes, the general structure of the interface remains the same.

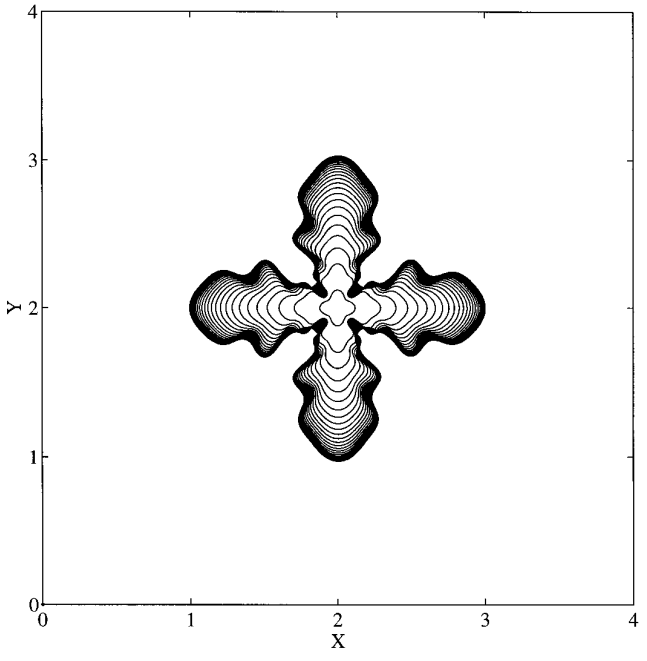

FIG. 18. Growth of a two-dimensional succinonitrile dendrite. At a length scale of $Z = 0.01$ cm, the thermal properties of succinonitrile [84] correspond to $\sigma = 2.8 \times 10^{-5}$, $\mu = 2.46 \times 10^{-4}$, $c_l/c_s = k_l/k_s \approx 1$. The undercooling St $= -0.1$ corresponds to -2.31 K. The growth of the four arms is symmetric and the features are well resolved. One can see the beginnings of side branch development; however, for such a low undercooling the effect of the insulated walls is felt early in the computation and slows the growth dramatically. $A_s = 0.08$, $m_s = 4$, $A_k = 0$.

eral of the liquid islands have circularized due to the effect of surface tension. The smaller islands eventually completely solidify. Comparison between this figure and Fig. 15 shows that, other than the topological changes, the general structure of the interface remains the same.

In Fig. 18 we attempt to simulate the growth of a fourfold symmetric ($m_s = 4$) succinonitrile dendrite. We do not expect to obtain agreement with experimental results since our simulation is for a two-dimensional domain with insulated boundaries. We want to demonstrate that we can achieve qualitatively realistic results using realistic values of the physical parameters. If we choose a length scale of $Z = 0.01$ cm then the thermal properties of succinonitrile [84] correspond to $\sigma = 2.8 \times 10^{-5}$, $\mu = 2.46 \times 10^{-4}$, $c_l/c_s = k_l/k_s \approx 1$ with a negligible density change upon solidification. The undercooling St $= -0.1$ corresponds to -2.31 K. The magnitude of the capillary anisotropy is $A_s = 0.08$ which is in the range of values reported in [85, 86]. There is no anisotropy in the kinetic mobility. We note that the form of the anisotropic capillary parameter used in the above references is

$$\sigma_n(\theta) = \sigma[1 - A_s \cos(4\theta)] \tag{41}$$

which is slightly different than Eq. (14). The interfaces in Fig. 18 are plotted at equal increments of $t = 0.2$ and the last interface shown is at $t = 4.6$. The growth of the four arms in Fig. 18 is symmetric and the features are well resolved. One can see the beginnings of side branch development; however, for such a low undercooling the effect of the insulated walls is felt early in the computation and slows the growth dramatically.

4. CONCLUSIONS

We have presented a new front-tracking method for stable and unstable solidification of pure substances based on standard finite difference techniques. Using a simple iterative algorithm, we solve the governing phenomenological equations and interface conditions directly and thus avoid introducing additional nonphysical simulation parameters. New features of the method include concepts from the immersed boundary technique to transfer information between the moving front and the stationary temperature grid and the construction of an indicator function which enables computations with discontinuous material properties. The method is also easily able to simulate surface tension and kinetic mobility anisotropies as well as topology changes.

We find that the method performs well when compared to exact solutions for stable solidification by a line heat sink. Grid resolution studies for computations of dendritic structures indicate that the method converges well under grid refinement. Although the physical features are well resolved, the effect of larger grid noise at lower resolutions acts to trigger the physical instabilities at earlier times. The results are shown to be free of any grid-induced anisotropy and grid orientation effects. As a test of thermodynamic consistency, we have simulated the critical nucleation radius to within 1% and have also matched the maximum theoretical solid fraction for solidification in an insulated cavity. For more unstable parameters, in particular for high St, low σ, or high c_l/c_s, the interface complexity and, thus, the required resolution increases. Although the method is, thus, eventually limited by resolution for highly unstable sets of parameters, we have achieved converged results for realistic values. The results in this work are limited to two dimensions, however, and are not directly comparable to three-dimensional experimental results.

For unstable, dendritic solidification with discontinuous material properties, we have found that the interface grows faster with an increase in the liquid to solid thermal conductivity and volumetric heat capacity ratios. In addition, with a small increase in the heat capacity ratio, the solid grows faster and the interface becomes more unstable than would be expected by an analysis of similar conditions in stable solidification. We identify two mechanisms which contribute to and magnify this instability. Our results indicate that

in modeling growth rates and interface morphology in the dendritic solidification of water and many pure metals, the discontinuity of material properties between liquid and solid phases is an important consideration. To our knowledge, similar computations which fully take into account unequal thermal conductivity and heat capacity have not previously been reported.

The main objective of the present work was to develop and verify the numerical method. In future work, we hope to extend the capability of the method to perform fully three-dimensional computations of dendritic solidification and thereby make comparisons with experimental results. The main difficulties in three-dimensional simulations are the computational requirements and the more complex surface tracking algorithms. However, such surface tracking has successfully been implemented in [74–76], for example. Due to the high computational expense the method will most likely need to incorporate adaptive mesh routines which allow finer resolution near the interface and also second-order time integration for increased accuracy in long time simulations.

ACKNOWLEDGMENTS

This work was supported in part by NSF Grant CTS-913214 and by NASA Graduate Student Fellowship NGT-51070. We acknowledge constructive interactions with Dr. D. Jacqmin at the NASA Lewis Research Center. D.J. thanks the University of Michigan for support through the Amoco Fellowship during the early phase of this research.

REFERENCES

1. H. Carslaw and J. Jaeger, *Conduction of Heat in Solids* (Clarendon Press, Oxford, 1959), p. 294.
2. H. G. Landau, *Q. Appl. Math.* **8,** 81 (1950).
3. M. E. Rose, *Math. Comput.* **14,** 249 (1960).
4. V. R. Voller, M. Cross, and P. Walton, in *Numerical Methods in Thermal Problems,* edited by R. W. Lewis and K. Morgan (Pineridge Press, Swansea, 1979), p. 172.
5. V. R. Voller and M. Cross, *Int. J. Heat Mass Transfer* **24,** 545 (1981).
6. C. R. Swaminathan and V. R. Voller, *Int. J. Numer. Methods. Heat Fluid Flow* **3,** 233 (1993).
7. G. Comini, C. Nonino, and O. Saro, in *Advanced Computational Methods in Heat Transfer. Vol. 3. Phase Change and Combustion Simulation,* edited by L. C. Wrobel, C. A. Brebbia, and A. J. Nowak (Springer-Verlag, Berlin, 1990), p. 3.
8. V. R. Voller and C. R. Swaminathan, *Int. J. Numer. Methods. Eng.* **30,** 875 (1990).
9. V. R. Voller and C. R. Swaminathan, *Numer. Heat Transfer, Part B* **19,** 175 (1991).
10. J. Crank and R.D. Phahle, *Bull. J. Inst. Math. Appl.* **9,** 12 (1973).
11. A. N. Alexandrou, *Int. J. Numer. Methods. Eng.* **28,** 2383 (1989).
12. K. O'Neill and D. R. Lynch, *Numerical Methods in Heat Transfer,* edited by R. W. Lewis, K. Morgan, and O. C. Zinkiewicz (Wiley, New York, 1981), Chap. 11.
13. W. W. Mullins and R. F. Sekerka, *J. Appl. Phys.* **35,** 444 (1964).
14. V. V. Voronkov, *Sov. Phys. Solid State* **6,** 2378 (1965).
15. W. W. Mullins and R. F. Sekerka, *J. Appl. Phys.* **34,** 323 (1963).
16. J. W. Cahn, in *Crystal Growth,* edited by H. S. Peiser (Pergamon, Oxford, 1967), p. 681.
17. S. R. Coriell and R. L. Parker, in *Crystal Growth,* edited by H. S. Peiser (Pergamon, Oxford, 1967), p. 703.
18. G. P. Ivantsov, *Dokl. Akad. Nauk. SSSR* **58,** 567 (1947).
19. D. E. Temkin, *Dokl. Akad. Nauk. SSSR* **132,** 1307 (1960).
20. G. F. Bolling and W. A. Tiller, *J. Appl. Phys.* **32,** 2587 (1961).
21. R. Trivedi, *Acta Metall.* **18,** 287 (1970).
22. M. E. Glicksman and R. J. Schaefer, *J. Crystal Growth* **1,** 297 (1967).
23. M. E. Glicksman and R. J. Schaefer, *J. Crystal Growth* **2,** 239 (1968).
24. M. E. Glicksman and S. P. Marsh, in *Handbook of Crystal Growth, Vol. 1B,* edited by D. T. J. Hurle (North-Holland, Amsterdam, 1993), p. 1075.
25. G. E. Nash and M. E. Glicksman, *Acta Metall.* **22,** 1283 (1974).
26. G. E. Nash and M. E. Glicksman, *Acta Metall.* **22,** 1291 (1974).
27. J. S. Langer and H. Müller-Krumbhaar, *J. Crystal Growth* **42,** 11 (1977).
28. J. S. Langer and H. Müller-Krumbhaar, *Acta Metall.* **26,** 1681 (1978).
29. J. S. Langer and H. Müller-Krumbhaar, *Acta Metall.* **26,** 1689 (1978).
30. J. S. Langer and H. Müller-Krumbhaar, *Acta Metall.* **26,** 1697 (1978).
31. M. E. Glicksman, M. B. Koss, and E. A. Winsa, *Phys. Rev. Lett.* **73,** 573 (1994).
32. M. E. Glicksman, M. B. Koss, L. T. Bushnell, J. C. LaCombe, R. N. Smith, and E. A. Winsa, in *Heat Transfer in Microgravity Systems,* HTD, Vol. 290, edited by S. S. Sadhal and A. Gopinath (ASME, New York, 1994), p. 1.
33. D. Kessler, J. Koplik, and H. Levine, *Phys. Rev. A* **34,** 4980 (1986).
34. D. Kessler, J. Koplik, and H. Levine, *Adv. Phys.* **37**(3), 255 (1988).
35. J.S. Langer, in *Chance and Matter,* edited by J. Souletie, J. Vannimenus, and R. Stora (North-Holland, Amsterdam, 1987), p. 629.
36. J. S. Langer, *Science* **243,** 1150 (1989).
37. P. Pelcé, *Dynamics of Curved Fronts* (Academic Press, New York, 1988).
38. J. P. Gollub, in *Nonlinear Phenomena Related to Growth and Form,* edited by M. Ben Amar, P. Pelcé, and P. Tabeling (Plenum, New York, 1991).
39. W. Kurz and R. Trivedi, *Acta Metall. Mater.* **38,** 1 (1990).
40. Y. Miyata, M. E. Glicksman, and S. H. Tirmizi, *J. Crystal Growth* **110,** 683 (1991).
41. E. R. Rubinstein and M. E. Glicksman, *J. Crystal Growth* **112,** 84 (1991).
42. E. R. Rubinstein and M. E. Glicksman, *J. Crystal Growth* **112,** 97 (1991).
43. J. M. Sullivan Jr., D. R. Lynch, and K. O'Neill, *J. Comput. Phys.* **69,** 81 (1987).
44. J. M. Sullivan Jr. and D. R. Lynch, *Int. J. Numer. Methods Eng.* **25,** 415 (1988).
45. J. M. Sullivan Jr. and H. Hao, in *Heat Transfer in Melting, Solidification and Crystal Growth,* HTD, Vol. 234, edited by I. S. Habib and S. Thynell (ASME, New York, 1993), p. 14.
46. K. H. Tacke, in *Free Boundary Problems: Theory and Applications, Vol. II,* edited by K. H. Hoffmann and J. Sprekels (Longman Sci. Tech., Essex, UK, 1990), p. 636.
47. J. A. Sethian and J. Strain, *J. Comput. Phys.* **98**(2), 231 (1992).
48. R. Almgren, *J. Comput. Phys.* **106,** 337 (1993).
49. A. R. Roosen and J. E. Taylor, *J. Comput. Phys.* **114,** 113 (1994).

50. W. Shyy, H. S. Udaykumar, and S.-J. Liang, *Int. J. Heat Mass Transfer* **36**(7), 1833 (1993).
51. K. Brattkus and D. I. Meiron, *SIAM J. Appl. Math.* **52**(5), 1303 (1992).
52. J. S. Langer, in *Directions in Condensed Matter Physics*, edited by G. Grinstein and G. Mazenko (World Scientific, Singapore, 1986), p. 164.
53. G. Fix, in *Free Boundary Problems,* edited by A. Fasano and M. Primocerio (Pitman, London, 1983), p. 580.
54. G. Caginalp, *Arch. Rat. Mech. Anal.* **92,** 205 (1986).
55. G. Caginalp, *Phys. Rev. A* **39,** 5887 (1989).
56. G. Caginalp, in *Free Boundary Problems Involving Solids,* edited by J. M. Chadam and H. Rasmussen (Longman Sci. Tech., Essex, UK, 1993), p. 92.
57. G. Caginalp and P. Fife, *SIAM J. Appl. Math.* **48,** 506 (1988).
58. J. B. Collins and H. Levine, *Phys. Rev. B* **31,** 6119 (1985).
59. G. Caginalp and E. A. Socolovsky, *J. Comp. Phys.* **95**, 85 (1991).
60. G. Caginalp and E. A. Socolovsky, in *Free Boundary Problems Involving Solids,* edited by J. M. Chadam and H. Rasmussen (Longman Sci. Tech., Essex, UK, 1993), p. 100.
61. R. Kobyashi, *J. Jpn. Assoc. Cryst. Growth* **18**(2), 209 (1991). [Japanese]
62. R. Kobyashi, in *Pattern Formation in Complex Dissipative Systems,* edited by S. Kai (World Scientific, Singapore, 1992), p. 121.
63. R. Kobyashi, *Physica D* **63,** 410 (1993).
64. A. A. Wheeler, in *Handbook of Crystal Growth, Vol. 1B,* edited by D. T. J. Hurle (North-Holland, Amsterdam, 1993), p. 683.
65. O. Penrose and P. Fife, *Physica D* **43,** 44 (1990).
66. S.-L.Wang, R. F. Sekerka, A. A. Wheeler, B. T. Murray, S. R. Coriell, R. J. Braun, and G. B. McFadden, *Physica D* **69,** 189 (1993).
67. A. A. Wheeler, B. T. Murray, and R. J. Schaefer, *Physica D* **66,** 243 (1993).
68. B. T. Murray, W. J. Boettinger, G. B. McFadden, and A. A. Wheeler, in *Heat Transfer in Melting, Solidification and Crystal Growth,* HTD, Vol. 234, edited by I. S. Habib and S. Thynell (ASME, New York, 1993), p. 67.
69. R. J. Braun, G. B. McFadden, and S. R. Coriell, *Phys. Rev. E* **49**(5), 4336 (1994).
70. N. M. H. Lightfoot, *Proc. London Math. Soc.* **31,** 97 (1929).
71. V. Alexiades and A. D. Solomon, *Mathematical Modeling of Melting and Freezing Processes* (Hemisphere, Washington, DC, 1993, p. 92.
72. V. Alexiades, A. D. Solomon, and D.G. Wilson, *J. Non-Equilib. Thermodyn.* **13,** 281 (1988).
73. D. Turnbull, *J. Appl. Phys.* **21,** 1022 (1950).
74. S. O. Unverdi, Ph.D. thesis, The University of Michigan, 1990.
75. S. O. Unverdi and G. Tryggvason, *Physica D* **60,** 70 (1992).
76. S. O. Unverdi and G. Tryggvason, *J. Comput. Phys.* **100**(1), 25 (1992).
77. Y.-J. Jan and G. Tryggvason, *Phys. Fluids,* submitted.
78. M. R. Nobari, Y.-J. Jan, and G. Tryggvason, *Phys. Fluids A,* submitted.
79. S. Nas and G. Tryggvason, in *AMD 174/FED 175 Fluid Mechanics Phenomena in Microgravity, 1993 ASME Winter Annual Meeting,* edited by D. A. Siginer, R. L. Thompson, and L. M. Trefethen, p. 71.
80. C. S. Peskin, *J. Comput. Phys.* **25,** 220 (1977).
81. C. S. Peskin, personal communication, 1993.
82. R. J. LeVeque and Z. Li, *SIAM J. Numer. Anal.* **31**(4), 1019 (1994).
83. E. A. Brandes and G.B. Brook (Eds.), *Smithells Metals Reference Book* (Butterworth, Heinemann, Oxford, UK, 1992), p. 14-1.
84. M. E. Glicksman, R. J. Schaefer, and J. D. Ayers, *Metall. Trans. A* **7A,** 1747 (1976).
85. M. E. Glicksman and N. B. Singh, in *Rapidly Solidified Powder Aluminum Alloys,* edited by M. E. Fine and E. A. Starke Jr. (ASTM, Philadelphia, PA, 1986), p. 44.
86. M. Muschol, D. Liu, and H. Z. Cummins, *Phys. Rev. A* **46,** 1038 (1992).